NATIONAL ADVISORY COMMITTEE FOR AERONAUTICS

TECHNICAL NOTE 4045

ELLIPTIC CONES ALONE AND WITH WINGS

AT SUPERSONIC SPEEDS

By Leland H. Jorgensen

Ames Aeronautical Laboratory
Moffett Field, Calif.

NACA

Washington
October 1957

.D

NATIONAL ADVISORY COMMITTEE FOR AERONAUTIC

TECHNICAL NOTE 4045

ELLIPTIC CONES ALONE AND WITH WINGS

AT SUPERSONIC SPEEDS

By Leland H. Jorgensen

SUMMARY

To help fill the gap in the knowledge of aerodynamics of shapes
intermediate between bodies of revolution and flat triangular wings, force
and moment characteristics for elliptic cones have been experimentally
determined for Mach numbers of 1.97 and 2.94. Elliptic cones having cross-
sectional axis ratios from 1 through 6 and with lengths and base areas
equal to circular cones of fineness ratios 3.67 and 5 have been studied
for angles of bank of 0° and 90°. Elliptic and circular cones in combina-
tion with triangular wings of aspect ratios 1 and 1.5 also have been con-
sidered. The angle-of-attack range was from 0° to about 16°, and the
Reynolds number was 8×10^6, based on model length. In addition to the
forces and moments at angle of attack, pressure distributions for elliptic
cones at zero angle of attack have been determined.

The results of this investigation indicate that there are distinct
aerodynamic advantages to the use of elliptic cones. With their major
cross-sectional axes horizontal, they develop greater lift and have higher
lift-drag ratios than circular cones of the same fineness ratio and volume.
In combination with triangular wings of low aspect ratio, they also develop
higher lift-drag ratios than circular cones with the same wings. For
winged elliptic cones, this increase in lift-drag ratio results both from
lower zero-lift drag and drag due to lift. Visual-flow studies indicate
that, because of better streamlining in the crossflow plane, vortex flow
is inhibited more for an elliptic cone with major axis in the plane of the
wing than for a circular cone with the same wing. As a result, vortex
drag resulting from lift is reduced. Shifts in center of pressure with
changes in angle of attack and Mach number are small and about the same
as for circular cones.

Comparisons of theoretical and experimental force and moment charac-
teristics for elliptic cones indicate that simple linearized (flat plate)
wing theory is generally adequate even for relatively thick cones. Zero-
lift pressure distributions and drag can be computed using Van Dyke's
second-order slender-body theory. For winged circular cones, a modifica-
tion of the slender-body theory of NACA Rep. 962 results in good agreement
of theory with experiment.

INTRODUCTION

Various theoretical studies have indicated that important aerodynamic advantages can result from the use of elliptic instead of circular cones for flight at supersonic speeds. At zero angle of attack, the pressure drag of a cone of given length and base area decreases as the cross section is changed from circular to flat elliptical (refs. 1 to 4). At angle of attack, theory predicts that elliptic cones produce large gains in lift and lift-drag ratio compared to circular cones (refs. 1, 5, and 6).

Although there is a moderate amount of theoretical information applicable to elliptic cones (particularly for the case of zero incidence), relatively little experimental data have been obtained. Except for some pressure-distribution data in references 7 and 8, all of the known experimental results have been presented by Rogers and Berry (ref. 9). For a Mach number of 1.41, they have studied pressure-distribution and force data for a series of relatively flat winglike elliptic cones having ratios of major-to-minor axes between 5.4 and 23.1.

In order to provide information for more bodylike shapes, the present experimental investigation was performed. The aerodynamic characteristics of a family of elliptic cones having ratios of major-to-minor axes between 1 and 6 were measured. Also included in this investigation is a study of the effects of adding triangular wings to circular and elliptic cones of given length and base area. The tests were made for Mach numbers of 1.97 and 2.94. The purpose of the present report is to discuss the resulting aerodynamic data and to compare theoretical and experimental results.

SYMBOLS

A aspect ratio, $\dfrac{4s^2}{A_w}$

A_b base area of cone, πab

A_p plan-form area of cone

A_w total wing plan-form area (including the part within the body)

a semimajor axis of elliptic cone

b semiminor axis of elliptic cone

c $\sqrt{a^2\cos^2\phi + b^2\sin^2\phi}$

C_{d_c} crossflow drag coefficient of cylinder

C_D drag coefficient, $\dfrac{D}{q_\infty A_b}$

C_{D_o} drag coefficient at zero lift

C_L lift coefficient, $\dfrac{L}{q_\infty A_b}$

$C_{L_{B_1}}$ lift coefficient for basic circular cone

C_m pitching-moment coefficient about base of cone, $\dfrac{\text{pitching moment}}{q_\infty A_b l}$

$C_{m_{B_1}}$ pitching-moment coefficient about base of basic circular cone

C_p pressure coefficient, $\dfrac{p-p_\infty}{q_\infty}$

D drag

d diameter of cone at base

E complete elliptic integral of second kind

l length of cone

L lift

$\left(\dfrac{L}{D}\right)_M$ maximum lift-drag ratio

$\left(\dfrac{L}{D}\right)_{M_{B_1}}$ maximum lift-drag ratio for basic circular cone

M_∞ free-stream Mach number

p_∞ free-stream static pressure

q_∞ free-stream dynamic pressure

s wing semispan, measured from body center line

x,y,z Cartesian coordinates as shown in figure 1

x_p center of pressure measured from cone vertex

y_s half the distance between flow separation lines on the cone at the base

y_v half the distance between vortex traces on the cone at the base

α angle of attack measured between body longitudinal axis and
           free-stream direction (see fig. 1)

β $\sqrt{M_\infty^2 - 1}$

ϵ wing semiapex angle

θ_s angle measured around base ellipse from horizontal base axis
           to flow separation line on cone

θ_v angle measured around base ellipse from horizontal base axis
           to vortex trace on cone

λ modification factor to take account of finite wing aspect ratios

ϕ angle of bank about body longitudinal axis (see fig. 1)

The positive directions of the angles and coefficients are shown in figure 1.

APPARATUS AND TESTS

Wind Tunnels

The experimental investigation was conducted in the Ames 1- by 3-foot supersonic wind tunnels no. 1 and no. 2. Tunnel no. 1 is a closed-circuit, continuous-operation type and is equipped with a flexible-plate nozzle that provides a variation of Mach number from 1.4 to 4.0. The Reynolds number is changed by varying the total pressure within the approximate limits of 1/5 of an atmosphere to 4 atmospheres. Tunnel no. 2 is a nonreturn, intermittent-operation type and is also equipped with a flexible-plate nozzle that provides a variation of Mach number from 1.4 to 3.8. Air for this tunnel is obtained from the Ames 12-foot wind tunnel at a pressure of about 6 atmospheres and is expanded through the nozzle to the atmosphere. Changes in Reynolds number are obtained by varying the total pressure.

Except for vapor-screen tests, the water content of the air in the 1- by 3-foot wind tunnels is maintained at less than 0.0003 pound of water per pound of dry air. Consequently, the effect of humidity on the flow is negligible.

Models

Plan-form and end views of the models studied are shown in figure 2. Three elliptic-cone bodies (B_2, B_3, and B_4) with a/b ratios of 1.5, 3, and 6 had the same length and base area as the basic circular cone (B_1).

Hence, the fineness ratio of $l/d = 3.67$ for the circular cone was also the equivalent fineness ratio for these elliptic cones. In order to check the effect of fineness ratio on the aerodynamic characteristics, an additional elliptic cone body (B_5) with an a/b ratio of 1.5 and a fineness ratio of 5 was also studied.

In addition to being tested alone, bodies B_1 ($a/b = 1$, $l/d = 3.67$) and B_3 ($a/b = 3$, $l/d = 3.67$) were also tested with triangular wings (W_1 and W_2) of aspect ratio 1 and 1.5. With the major cross-sectional axis (a) of body B_3 mounted horizontally in line with the wings, the configurations are designated as $B_{3H}W_1$ and $B_{3H}W_2$. With the major axis of B_3 vertical to the wings, the configurations are designated as $B_{3V}W_1$ and $B_{3V}W_2$. The wing sections were flat plates with leading and trailing edges beveled as shown in figure 2.

All of the models were sting supported from the rear. Bodies B_3 and B_4 had pressure orifices distributed over the surfaces and were adaptable for both force and pressure-distribution tests.

<div align="center">Tests</div>

Force and pressure-distribution tests.- Force data were obtained in tunnel no. 2 for all the models at free-stream Mach numbers of 1.97 and 2.94. The Reynolds number, which was maintained constant for all tests, was 8×10^6 based on body length. Measurements of lift, drag, and pitching moment were taken for angles of attack from 0° to about 16°. The elliptic-cone bodies were tested at angles of bank of 0° and 90° (i.e., for $\phi = 0^\circ$ and 90° as shown in fig. 1). The winged elliptic cones were tested only with their wings at $\phi = 0^\circ$. Base pressures from eight orifices spaced around the inside of the base periphery of each body were measured by photographic recording from a multiple-tube manometer board.

Pressure-distribution data were obtained in tunnel no. 1 for bodies B_3 and B_4 at zero angle of attack and Mach number 1.97. The surface pressures were measured by photographic recording from a multiple-tube manometer system. The repeatability of both force and pressure measurements was checked by making reruns for several configurations.

Vapor-screen tests.- To make the vortices shed from the models at angle of attack visible, the "vapor-screen" method (ref. 10) was used. With this technique, water vapor is added to the tunnel air stream. This water vapor condenses in the wind-tunnel test section to produce a fine fog. A narrow sheet of bright light, produced by high-intensity mercury-vapor lamps, is projected through the tunnel window in a plane perpendicular to the model longitudinal axis. This plane of light appears as a uniformly lighted screen of fog particles in the absence of a model. However, with a model in the stream, the flow about the model affects the light scattered by the water particles, and vortices shed from the model are visible as dark spots.

Vapor-screen tests were made in tunnel no. 1 for various models at Mach number 1.97 and a Reynolds number of 8×10^6. With the models at several angles of attack, the vortex patterns were photographed with a camera mounted inside the wind tunnel 9 inches downstream from the base of the models.

Sublimation tests.- Another method of flow visualization that was used was the sublimation technique (ref. 11) for determining boundary-layer transition, flow separation, and vortex traces on the surfaces of the models. The models of this investigation, which were initially painted black, were sprayed with a 4-percent solution of acenaphthene in petroleum ether. This solution dries on contact with the model surface and presents a white appearance. The wind tunnel is operated, and as the process of sublimation takes place with the model in the tunnel, evidences of boundary-layer transition, separation, and vortex flow appear on the model. Regions of high surface shear, such as turbulent boundary layers and vortex traces, show up as dark areas, whereas regions of laminar flow and separation remain white. All sublimation tests were made in tunnel no. 1 at Mach number 1.97.

REDUCTION AND ACCURACY OF DATA

All of the pressure-distribution, force, and moment data have been reduced to coefficient form and are referred to the coordinate system shown in figure 1. The base drag was computed using the average base pressure and was subtracted from the total axial-force balance measurement, so that the data presented are for forces ahead of the body base.

The accuracy of the final data is affected by uncertainties in the measurement of the pressures, forces, and moments, and in the determination of the stream static and dynamic pressures used in reducing the data to coefficient form. These individual uncertainties led to estimated uncertainties which are listed in the following table:

Coefficient	Uncertainty
C_p	± 0.004
C_L	$\pm .02$
C_D	$\pm .004$
C_m	$\pm .02$
x_p/l	$\pm .02$

The values of angle of attack are estimated to be accurate to within $\pm 0.1^\circ$. The variation of the free-stream Mach number in the region of the test models was less than ± 0.01 at Mach number 1.97 and less than ± 0.02 at Mach number 2.94.

RESULTS AND DISCUSSION

This section of the report is divided into three parts: (1) experimental force and moment characteristics; (2) comparisons of theoretical and experimental pressure distributions, forces, and moments; and (3) visual observations of the flow over various models. The experimental force and moment characteristics are presented in figures 3 through 9; comparisons of theory and experiment are presented in figures 10 through 17; and photographs and measurements from the visual-flow studies are presented in figures 18 through 22.

Experimental Force and Moment Characteristics

Effect of axis ratio (a/b).- The effect of change in cross-sectional axis ratio (a/b) on the aerodynamic characteristics of the elliptic cones of fineness ratio 3.67 is presented in figures 3 and 4 for Mach numbers 1.97 and 2.94. Plan-form and end-view sketches of the models tested are used to identify each curve. For the models banked 90° the curves are labeled $\phi = 90°$, whereas for the models at zero bank the curves are unlabeled, a practice followed throughout the report. For the elliptic cones of figures 3 and 4 the lengths and base areas are constant; hence increases in a/b result in increases in plan-form area with the major axis, a, horizontal ($\phi = 0°$) and decreases in plan-form area with the major axis vertical ($\phi = 90°$). In view of this fact, it is not surprising that with increase in a/b the lift coefficients (which are referred to base area) increase appreciably at all angles of attack for $\phi = 0°$ and decrease for $\phi = 90°$ (figs. 3(a) and 4(a)). The question arises, then, of whether or not the aerodynamic efficiency as determined by the lift-drag ratio can also be markedly increased by increasing a/b. From figures 3(c) and 4(c) it is clear that, at least throughout the angle-of-attack range investigated, significant gains in lift-drag ratio can be realized by increasing a/b from 1 to 6. In fact, by merely changing a/b from 1 to 1.5 a gain in maximum L/D of about 25 percent results. Furthermore, increasing a/b from 1 to 3 results in about a 75-percent increase in maximum L/D at Mach number 1.97 and in about a 60-percent increase at Mach number 2.94. It is clear that, in many cases where a body of given volume is required, it can be aerodynamically beneficial to deviate from a circular cross section.

The effect of axis ratio on pitching moment and center of pressure is shown in figures 3(d), 3(e), 4(d), and 4(e). For all of the elliptic cones the center of pressure moves very little with angle of attack. With the major axis horizontal the center of pressure changes little with a/b and, as for the circular cone, is located at about the centroid of plan-form area for both Mach numbers 1.97 and 2.94. However, with the cones rotated to $\phi = 90°$, the center of pressure moves rearward from the centroidal position with increase in a/b from 1 to 6.

Effect of fineness ratio.- The effect of change in fineness ratio on
the aerodynamic characteristics of elliptic cones of $a/b = 1.5$ is illus-
trated in figure 5. Data are compared for body B_2 of $l/d = 3.67$ and
body B_5 of $l/d = 5$ tested at Mach numbers 1.97 and 2.94. For angles
of attack to about $8°$ there is little effect of fineness ratio on the lift
(fig. 5(a)). At higher angles, however, the lift coefficients are greater
for the more slender cone (B_5). For all values of C_L the drag coeffi-
cients for B_5 were at least 20 percent lower than for B_2 (fig. 5(b)).
It is not surprising, then, that an increase in fineness ratio also
results in substantially higher values of maximum lift-drag ratio. (See
fig. 5(c).) Although the lift, drag, and pitching-moment results were
affected by change in fineness ratio, there was no effect on center of
pressure, x_p/l (fig. 5(d)).

It is interesting to note that there is an effect of Mach number on
maximum lift-drag ratio which depends upon fineness ratio. For body B_2
of $l/d = 3.67$ the maximum value of L/D decreases with increase in Mach
number from 1.97 to 2.94, whereas for body B_5 of $l/d = 5$ the maximum
value of L/D increases (fig. 5(c)).

Effect of axis ratio (a/b) and arrangement for winged elliptic cones.-
For conical bodies alone it has been shown that use of elliptic cross
sections results in worthwhile gains in lift and lift-drag ratio. It is
not clear, however, whether significant gains also can be realized through
the use of elliptic cross sections for winged conical bodies. The test
results presented in figures 6 through 9 demonstrate that important aero-
dynamic advantages can be obtained through proper arrangement of an ellip-
tic body with a triangular wing. For instance, as shown in figures 6
and 7, gains in lift and large gains in lift-drag ratio result from using
an elliptic body ($a/b = 3$) with the major axis, a, in the plane of an
aspect ratio 1 wing in preference to a circular body with the same wing.
(Compare results for $B_{3H}W_1$ and B_1W_1.) However, with the elliptic body
rotated $90°$ so that the minor axis is in the plane of the wing (model
$B_{3V}W_1$), a loss in lift-drag ratio results. The gain in L/D for $B_{3H}W_1$
and loss in L/D for $B_{3V}W_1$ is primarily attributable to differences
in drag (figs. 6(b) and 7(b)). Because of less wetted surface area and
hence less skin friction, $B_{3H}W_1$ has slightly lower drag at zero lift
than the other configurations. With increase in lift, $B_{3H}W_1$ still has
the least drag, but the difference in drag between the models increases,
resulting in a significantly higher value of maximum L/D for $B_{3H}W_1$
than for B_1W_1 or $B_{3V}W_1$. For the same bodies with a wing of aspect
ratio 1.5 instead of 1, the differences between the maximum lift-drag
ratios are diminished. (See figs. 8(c) and 9(c).) However, the results
still significantly favor a body of elliptic cross section with the major
axis in the plane of the wing.

The maximum lift-drag ratios were higher for the elliptic cones with
major axes in line with the wings, primarily because they have less zero-
lift drag and develop less drag due to lift. It is believed that the
lower drag due to lift can be attributed to less vortex drag associated
with the formation of vortices at angle of attack. From visual observa-
tions of the flow over the models by the vapor-screen technique, it was

found that, at least for angles of attack from $0°$ to about $10°$, the formation of vortices was inhibited more with the major axis of an elliptic cone in line with a wing (model $B_{3H}W_1$) than perpendicular to it (model $B_{3V}W_1$). Vortices appeared to separate from $B_{3V}W_1$ and B_1W_1 at lower angles of attack than from $B_{3H}W_1$. It is interesting to note that, as shown in the vapor-screen photographs of figure 20(a) to be discussed later, the vortices shed from $B_{3V}W_1$ and B_1W_1 at $\alpha = 10°$ appeared to be more completely formed and rolled up than those for $B_{3H}W_1$. As shown in figures 6 and 7, the drag due to lift is higher for $B_{3V}W_1$ and B_1W_1 at $\alpha = 10°$ than for $B_{3H}W_1$. Apparently because of better streamlining in the crossflow plane, the vortex formation is inhibited and the drag due to lift is reduced with the major axis of the elliptic cone in line with the wing.

Comparisons of Theoretical and Experimental Pressure Distributions, Forces, and Moments

In this section of the report, theoretical methods of estimating the aerodynamic characteristics are assessed by comparison of theoretical results with experimental data. All comparisons are presented in figures 10 through 17 and are discussed in the following paragraphs.

Pressure distributions and drag of elliptic cones at zero angle of attack.- For elliptic cones of a/b of 3 and 6 (B_3 and B_4) theoretical and experimental pressure distributions for a Mach number of 1.97 are compared in figure 10. The pressure coefficients are plotted as a function of lateral distance, y/a, over a quadrant of each cone. The fact that the flow was conical is verified by the multiple experimental points at several y/a positions which were obtained at different longitudinal positions. The comparisons show that best agreement of theory with experiment is obtained through use of the second-order slender-body theory of Van Dyke (ref. 4). Both the slender-body theory of references 1 and 2 and the not-so-slender-body theory of reference 4 result in pressure coefficients which are lower than those of experiment. Rogers and Berry (ref. 9) also found the agreement of second-order slender-body theory with experiment to be quite good for elliptic cones having even higher ratios of a/b.

A study of the effect of change in axis ratio (a/b) on the zero-lift drag of elliptic cones is summarized in figure 11. The experimental results show that for these cones of equal volume and fineness ratio the drag remains essentially constant with change in axis ratio (a/b) at both Mach numbers 1.97 and 2.94. The boundary-layer flow over the models was mostly turbulent as shown by the sublimation results (to be discussed later) and as indicated by drag measurements with and without a transition ring at the nose of models B_1 and B_3. As seen in figure 11, the zero-lift drag is adequately predicted by the addition of turbulent skin friction (ref. 12) to pressure drag calculated by second-order slender-body

theory (ref. 4). For the circular cone (B_1) the drag is also closely
given by the addition of turbulent skin-friction drag (ref. 12) to pres-
sure drag by Taylor-Maccoll cone theory (ref. 13). It is noted that the
increase in skin-friction drag with increase in a/b (because of greater
wetted surface area) is just large enough to nullify the drag saving from
the decrease in pressure drag.

Forces and moments for elliptic cones.- Theoretical and experimental
force and moment characteristics for elliptic cones at Mach numbers 1.97
and 2.94 are compared in figures 12 and 13. Both slender-body theory
(refs. 1 and 5) and linearized wing theory (ref. 14) have been used in
computing the theoretical values of lift, drag, and pitching-moment coef-
ficients shown. In computing the drag coefficient at angle of attack,
the following expression has been used:

$$C_D = C_{D_O} + \left(\frac{dC_L}{d\alpha}\right)\alpha^2 \tag{1}$$

where

$$\frac{dC_L}{d\alpha} = \frac{C_L}{\alpha}$$

This relationship results from assuming that C_L varies linearily with
α and that there is flow separation along the leading edges with complete
loss of suction force. Theoretical values of C_D have been computed by
assuming $dC_L/d\alpha$ to be given both by slender-body theory and by linearized
wing theory. As discussed in the previous section, the drag coefficient at
zero angle of attack (C_{D_O}) was computed from the addition of turbulent
skin-friction drag (ref. 12) to pressure drag by second-order slender-body
theory (ref. 4). As shown in figures 12 and 13, the agreement with experi-
ment of the force and moment characteristics computed by means of linear-
ized wing theory is generally quite good, especially for angles of attack
from 0° to about 10°.

In figure 14 theoretical and experimental lift-curve slopes are com-
pared. Results are correlated by plotting the parameter of lift-curve
slope $\frac{\beta}{4}\left(\frac{dC_L}{d\alpha}\right)\left(\frac{A_b}{A_p}\right)$ as a function of the ratio of leading-edge slope to
Mach wave slope $\beta \tan \epsilon$. Except for bodies B_3 and B_4 at $\phi = 90^O$ and
$M_\infty = 2.94$, the experimental data agree closely with linearized (flat
plate) wing theory. Bodies B_3 (a/b = 3) and B_4 (a/b = 6) banked to
$\phi = 90^O$ are very thick in the lift direction, and at $M_\infty = 2.94$ their
lift-curve slopes are considerably higher than those given by either
slender-body or linearized wing theory.

The nonlinearity of the experimental lift and pitching-moment curves
(figs. 12 and 13), which becomes more evident at angles of attack greater
than about 10°, probably results from viscous crossflow separation. Allen
(ref. 10) has shown that for slender bodies of revolution an allowance for

viscous effects can be computed. This is done by adding to the lift computed by slender-body or linearized theory an additional crossflow lift attributed to the separation effects of viscosity. Flax and Lawrence (ref. 15) have suggested the same procedure for low-aspect-ratio wings, and the resulting expression for lift coefficient is

$$C_L = \left(\frac{dC_L}{d\alpha}\right)_{\substack{\text{linear} \\ \text{theory}}} \alpha + C_{d_c} \frac{A_p}{A_b} \alpha^2 \tag{2}$$

where C_{d_c} is the drag coefficient of a two-dimensional cylinder of equivalent cross section placed normal to a stream at a Mach number of $M_\infty \sin \alpha$. For the elliptic cones of this investigation, the lift is greatly overestimated by the use of equation (2). To illustrate this fact, the lift for the circular cone (B_1) computed using equation (2) is compared with experiment in figure 12(a). The usual circular cylinder value of $C_{d_c} = 1.2$ was used. Rogers and Berry (ref. 9) in their study of elliptic cones of higher ratios of a/b also found that equation (2) leads to lift coefficients larger than those given by experiment.

Although the lift and pitching-moment results of figures 12 and 13 show moderate nonlinearity with increase in α, the data can be simply correlated as shown in figure 15. Here the lift and pitching-moment coefficients for the elliptic cones are divided by the corresponding coefficients for the equivalent circular cone, and the ratios are plotted as a function of α. The results of the correlation demonstrate that, in general, $C_L/C_{L_{B_1}}$ and $C_m/C_{m_{B_1}}$ remain constant with change in α. Except for the elliptic cone of a/b = 6 (B_4) at Mach number 2.94, the lift and moment ratios are given reasonably well by linearized wing theory.

Effect of axis ratio (a/b) on maximum lift-drag ratios of elliptic cones.- The effect of axis ratio (a/b) on the maximum lift-drag ratios of elliptic cones can be readily computed. From equation (1) the maximum lift-drag ratio is given by the relation

$$\left(\frac{L}{D}\right)_M = \frac{1}{2}\sqrt{\frac{C_L/\alpha}{C_{D_0}}} \tag{3}$$

If for cones of given fineness ratio it is assumed that C_{D_0} is constant with change in a/b (as suggested from the results of the present experiments), then the relative efficiency of an elliptic cone to a circular cone is expressed by the relation

$$\frac{(L/D)_M}{(L/D)_{M_{B_1}}} = \sqrt{\frac{C_L/\alpha}{(C_L/\alpha)_{B_1}}} \tag{4}$$

For slender-body theory this ratio reduces to

$$\frac{(L/D)_M}{(L/D)_{M_{B_1}}} = \sqrt{\frac{a}{b}\cos^2\phi + \frac{b}{a}\sin^2\phi} \tag{5}$$

since

$$C_L = 2\alpha\left(\frac{a}{b}\cos^2\phi + \frac{b}{a}\sin^2\phi\right)$$

In figure 16, computed values of $(L/D)_M$ and $(L/D)_M/(L/D)_{M_{B_1}}$ are compared with the experimental results for the cones of fineness ratio 3.67. The computations were made with values of C_L given both by slender-body theory and linearized wing theory. Since, as was shown in figure 11, the zero-lift drag was almost constant with change in a/b, average experimental values of C_{D_0} of 0.086 at $M_\infty = 1.97$ and 0.073 at $M_\infty = 2.94$ have been used in the calculations. In general, the agreement of theory with experiment is good, the best agreement being obtained with linearized wing theory. In the lower plot of figure 16, however, the comparisons show that the relative efficiency of an elliptic to a circular cone can be closely estimated by means of slender-body theory (eq. (5)) for moderate values of a/b (of the order of 3 or less).

Forces and moments for winged circular cones.- For a slender wing-body combination consisting of a triangular wing mounted on a circular cone so that their vertices coincide, the lift coefficient is given by the slender-body method of Spreiter (ref. 16) as

$$C_L = \frac{\pi}{2}A\sigma\frac{A_W}{A_b}\alpha \tag{6}$$

where

$$\sigma = 1 + \left(\frac{d}{2s}\right)^4 + \frac{1}{2\pi}\left\{\frac{d}{s}\left[1 - \left(\frac{d}{2s}\right)^2\right] - \left[1 + \left(\frac{d}{2s}\right)^2\right]^2\sin^{-1}\frac{\frac{d}{s}}{1 + \left(\frac{d}{2s}\right)^2}\right\}$$

It has been shown (refs. 16 and 17) that the slender-body method of Spreiter can be modified so as to give results comparable to linearized theory. For winged circular cones this is accomplished merely by multiplying equation (6) by a modification factor λ. This factor is the ratio of the lift of the wing alone by linearized theory to the lift by slender-body theory and is given by

$$\left.\begin{aligned}\lambda &= \frac{1}{E\left(\sqrt{1 - \beta^2\tan^2\epsilon}\right)}; & \beta\tan\epsilon \leq 1\\[2ex]\lambda &= \frac{2}{\pi\beta\tan\epsilon}; & \beta\tan\epsilon \geq 1\end{aligned}\right\} \tag{7}$$

By application of the factor λ to equation (6), there is obtained

$$C_L = \frac{\pi}{2} A\sigma\lambda \frac{A_w}{A_b} \alpha \tag{8}$$

Since the center of pressure is at the centroid of plan-form area, the pitching-moment coefficient is given by the relation

$$C_m = \frac{\pi}{6} A\sigma\lambda \frac{A_w}{A_b} \alpha \tag{9}$$

In figure 17, theoretical and experimental force and moment characteristics of winged circular cones are compared. Equations (8) and (9) were used to compute the lift and pitching-moment curves, and equations (1) and (8) to compute the lift-drag polars and ratios. The drag at zero lift was estimated by the addition of turbulent skin-friction drag (ref. 12) for the entire surface to the body pressure drag obtained by second-order slender-body theory (ref. 4). The agreement of the computed results with the experimental data is good for angles of attack below about 10°. As yet, the details of a method for computing the aerodynamic characteristics of winged elliptic cones have not been worked out.

Visual Observations of Flow Over Models

To supplement the force and moment results with studies that aid in giving a physical representation of the flow, vapor-screen and sublimation tests were made for the models at Mach number 1.97. Photographs and measurements of the resulting flow patterns are presented in figures 18 through 22. As mentioned previously, the vapor-screen pictures were taken with a camera mounted inside the tunnel just downstream of the models. The pictures of the models from the sublimation tests were taken immediately following tunnel shutdown.

Vapor-screen results.- In the photographs of figure 18, base views of bodies B_1, B_2, and B_3 showing vortices are presented for $\alpha = 10^\circ$, 15°, and 20°. For these pictures the light plane intersected the model axis at about $x = 0.7l$, and part of the flow field was in the shadow of the model. In figure 18 a symmetrical pair of vortices is shown above each model. These vortices, which originate at the nose, were observed to grow in size (and presumably strength) with travel from the nose to the base. At each axial length position, it was found that the sizes and positions of the vortices relative to the body cross section were practically the same. In figure 18 it is seen that the sizes of the vortex regions increase with increase in α from 10° to 20°. The vortex regions also flatten out and move outboard relative to the body vertical center line with increase in a/b above 1.

The photographs of figures 19(a) and 19(b) are presented in order to demonstrate the effect of angle of bank on the vortex regions associated

with elliptic cones at $\alpha = 15^\circ$ and 20°. For all cases studied, as the models were banked from $\phi = 0^\circ$ to $\phi = -45^\circ$ the right vortex region appeared to flatten out and lie nearer to the body surface.

In figure 20 pictures of vortex patterns for the winged cones of aspect ratio 1 (B_1W_1, $B_{3H}W_1$, and $B_{3V}W_1$) are shown. These pictures were taken with the light plane at about the base of each model. As for the elliptic cones without wings, the vortex regions above the winged cones increase in size with increase in α from 10° to 15°. With α kept constant at 15°, the right vortex region flattens out and moves nearer to the model surface with change in ϕ from 0° to -45° (fig. 20(b)). Comparison of these pictures with those for the bodies alone shows that the addition to a body of even low-aspect-ratio wings results in considerable outboard and downward movement of the vortex regions; for instance, compare the pictures for B_1 in figure 18 with those for B_1W_1 in figure 20. From these observations, it appears that body vortex interference with a vertical fin or air-breathing engine mounted above a body can be reduced by extending low-aspect-ratio wings all the way to the nose.

What is believed to be secondary vortex flow below and outboard of the main vortex regions is indicated in some of the photographs of the models at $\alpha = 20^\circ$. This is especially evident for model $B_{3H}W_1$ at $\alpha = 20^\circ$ in figure 20(a). This secondary vortex flow also has been observed for delta wings at supersonic speeds by Drougge and Larson (ref. 18).

Sublimation technique results.- Transition, separation, and vortex regions for models B_1, B_2, and B_3 are shown in the photographs of figure 21. Top, side, and bottom views for the models at an angle of attack of 15° are presented. As seen in the bottom views, the boundary-layer flow over the models was mostly turbulent, the laminar region being limited to the white area near the nose. In the side views a line indicating flow separation is shown for each model, and in the top views symmetrical vortex traces are visible. Although not clearly evident in the pictures, the separation lines and vortex traces extended almost linearly from the nose to the base of each model. Measurements of the symmetrical separation and vortex positions at the base of all of the body models of $l/d = 3.67$ were taken. In figure 22 the separation and vortex positions are plotted as a function of a/b. It is seen that for $a/b = 1.5$ with the model banked 90° so that the minor axis is horizontal, the separation lines and vortex traces are close together and near the top of the body. With the model unbanked ($\phi = 0^\circ$) so that the major axis is horizontal, the separation and vortex positions are farther apart and nearer the sides of the body. For unbanked cones with a/b greater than 3, the flow separation positions are essentially at the sides of the body, and the vortex traces are about midway between the sides and the top.

CONCLUSIONS

Aerodynamic characteristics of elliptic cones alone and with triangular wings have been measured for Mach numbers 1.97 and 2.94 at a Reynolds number of 8×10⁶, based on model length. Cones having fineness ratios (l/d) of 3.67 and 5 and cross-sectional axis ratios (a/b) from 1 through 6 have been considered for angles of bank of 0° and 90°. In addition, a study has been made of cones of l/d of 3.67 and a/b of 1 and 3 in combination with wings of aspect ratio 1 and 1.5. An analysis of the results has led to the following conclusions:

1. Pressure distributions over elliptic cones at zero incidence can be computed reasonably well by means of Van Dyke's second-order slender-body theory.

2. For a cone of given fineness ratio at zero lift, the pressure drag decreases with increase in cross-sectional axis ratio a/b. However, with a turbulent boundary layer, the skin friction increases enough that the pressure plus skin-friction drag remains practically constant with increase in a/b. The foredrag can be computed accurately by the addition of theoretical skin-friction drag to pressure drag predicted by second-order slender-body theory.

3. With the major cross-sectional axis horizontal, increases in axis ratio a/b result in large gains in lift and lift-drag ratio. These gains can be computed reasonably well by the use of linearized wing theory.

4. For a given cross-sectional axis ratio a/b, the lift-drag ratio increases with increase in equivalent fineness ratio.

5. For wing-body combinations, a body with an elliptic cross section instead of a circular cross section appears aerodynamically advantageous. With triangular wings (aspect ratio = 1, 1.5) mounted on cones $(l/d = 3.67)$ so that their vertices coincide, higher lift-drag ratios result from an elliptic cross section with major axis in line with the wings than from a circular cross section. However, a decrease in lift-drag ratio results from an elliptic cross section with the minor axis in line with the wing.

6. For the cones alone and with triangular wings, shifts in center of pressure with changes in angle of attack and Mach number are very small.

7. For winged circular cones, the theoretical results of NACA Rep. 962 can be modified to give good agreement with experimental results for angles of attack below about 10°.

8. Visual boundary-layer flow studies indicate that, for unbanked elliptic cones at angle of attack, a pair of symmetrical vortices start at the nose and trace a linear path to the base. These vortices increase

in size with travel from the nose to the base. The flow separation lines
from which the vortices are fed also trace an essentially linear path
along the model surface.

Ames Aeronautical Laboratory
        National Advisory Committee for Aeronautics
                Moffett Field, Calif., July 17, 1957

REFERENCES

1. Fraenkel, L. E.: Supersonic Flow Past Slender Bodies of Elliptic
        Cross Section. R. & M. No. 2954, British A.R.C., 1955.

2. Kahane, A., and Solarski, A.: Supersonic Flow About Slender Bodies
        of Elliptic Cross Section. Jour. Aero. Sci., vol. 20, no. 8,
        Aug. 1953, pp. 513-524.

3. Ferri, Antonio, Ness, Nathan, and Kaplita, Thaddeus T.: Supersonic
        Flow Over Conical Bodies Without Axial Symmetry. Jour. Aero. Sci.,
        vol. 20, no. 8, Aug. 1953, pp. 563-571.

4. Van Dyke, Milton D.: The Slender Elliptic Cone as a Model for
        Nonlinear Supersonic Flow Theory. Jour. Fluid Mech., vol. 1, no. 1,
        May 1956, pp. 1-15.

5. Ward, G. N.: Supersonic Flow Past Slender Pointed Bodies. Quart.
        Jour. Mech. and Appl. Math., vol. II, pt. 1, Mar. 1949, pp. 75-97.

6. Seaman, Donna Jean, and Dore, Frank J.: Force and Pressure Coeffi-
        cients of Elliptic Cones and Cylinders in Newtonian Flow.
        Rep. ZA-7-004, Consolidated Vultee Aircraft Corp., San Diego,
        May 16, 1952.

7. Maslen, Stephen H.: Pressure Distributions on Thin Conical Body of
        Elliptic Cross Section at Mach Number 1.89. NACA RM E8K05, 1949.

8. Ferri, Antonio: The Linearized Characteristics Method and Its
        Application to Practical Nonlinear Supersonic Problems. NACA
        TN 2515, 1951.

9. Rogers, E. W. E., and Berry, C. J.: Experiments at M = 1.41 on
        Elliptic Cones with Subsonic Leading Edges. British A.R.C. 17929,
        FM 2307, Perf. 1391, Oct. 11, 1955.

10. Allen, H. Julian, and Perkins, Edward W.: A Study of Effects of
        Viscosity on Flow Over Slender Inclined Bodies of Revolution.
        NACA Rep. 1048, 1951.

11. Main-Smith, J. D.: Chemical Solids as Diffusible Coating Films for Visual Indications of Boundary-Layer Transition in Air and Water. R. & M. No. 2755, British A.R.C., 1954.

12. Rubesin, Morris W., Maydew, Randall C., and Varga, Steven A.: An Analytical and Experimental Investigation of the Skin Friction of the Turbulent Boundary Layer on a Flat Plate at Supersonic Speeds. NACA TN 2305, 1951.

13. Ames Research Staff: Equations, Tables, and Charts for Compressible Flow. NACA Rep. 1135, 1953.

14. Stewart, H. J.: The Lift of a Delta Wing at Supersonic Speeds. Quart. Appl. Math., vol. IV, no. 3, Oct. 1946, pp. 246-254.

15. Flax, A. H., and Lawrence, H. R.: The Aerodynamics of Low-Aspect-Ratio Wings and Wing-Body Combinations. Third Anglo-American Aeronautical Conference, Brighton, 4th - 7th September 1951. Convened by the R.A.S. and I.A.S., Joan Bradbrooke and E. G. Pike, eds., 1952, pp. 363-398. (Published also as Rep. CAL-37, Cornell Aeronautical Lab., Inc., Buffalo, 1951)

16. Spreiter, John R.: The Aerodynamic Forces on Slender Plane- and Cruciform-Wing and Body Combinations. NACA Rep. 962, 1950.

17. Nielsen, Jack N., Katzen, Elliott D., and Tang, Kenneth K.: Lift and Pitching-Moment Interference Between a Pointed Cylindrical Body and Triangular Wings of Various Aspect Ratios at Mach Numbers of 1.50 and 2.02. NACA TN 3795, 1956.

18. Drougge, G., and Larson, P. O.: Pressure Measurememts and Flow Investigation on Delta Wings at Supersonic Speed. Flygtekniska Försöksanstalten, The Aeronautical Research Institute of Sweden, Rep. 57, Stockholm, Nov. 1956.
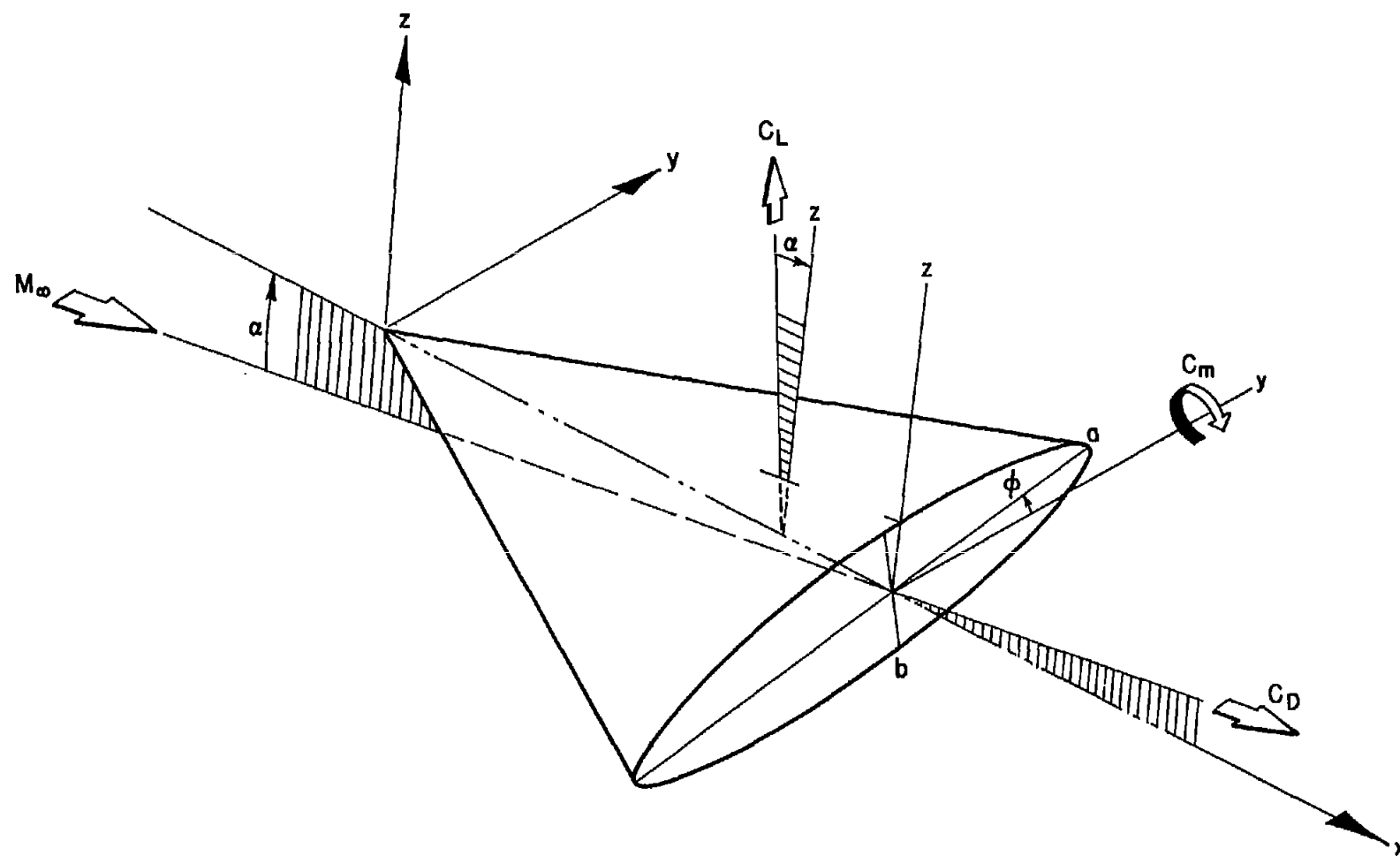
Figure 1.- Coordinate system and sign convention.

.005 d radius

.ld

.03d

.5d

.005 d radius

Typical leading edge
Section A-A (Enlarged)

Typical trailing edge
Section B-B (Enlarged)

$l = 9.90"$

d

B_1

$\frac{a}{b} = 1, \frac{l}{d} = 3.67, \frac{a}{d} = .50$

b

a

B_2

$\frac{a}{b} = 1.5, \frac{l}{d} = 3.67, \frac{a}{d} = .61$

B_3

$\frac{a}{b} = 3, \frac{l}{d} = 3.67, \frac{a}{d} = .87$

B_4

$\frac{a}{b} = 6, \frac{l}{d} = 3.67, \frac{a}{d} = 1.22$

B_5

$\frac{a}{b} = 1.5, \frac{l}{d} = 5, \frac{a}{d} = .61$

$B_1 W_1$

d

2s

$\frac{a}{b} = 1, \frac{l}{d} = 3.67, A = 1, 2\frac{s}{d} = 1.84$

$B_{3H} W_1$

$\frac{a}{b} = 3, \frac{l}{d} = 3.67, A = 1, 2\frac{s}{d} = 1.84$

$B_{3V} W_1$

$\frac{a}{b} = 3, \frac{l}{d} = 3.67, A = 1, 2\frac{s}{d} = 1.84$

A-A   B-B

$B_1 W_2$

d

2s

$\frac{a}{b} = 1, \frac{l}{d} = 3.67, A = 1.5, 2\frac{s}{d} = 2.76$

$B_{3H} W_2$

$\frac{a}{b} = 3, \frac{l}{d} = 3.67, A = 1.5, 2\frac{s}{d} = 2.76$

$B_{3V} W_2$

$\frac{a}{b} = 3, \frac{l}{d} = 3.67, A = 1.5, 2\frac{s}{d} = 2.76$

Figure 2.- Plan-form and end views of configurations.

(a) Lift.

(b) Lift-drag polar.
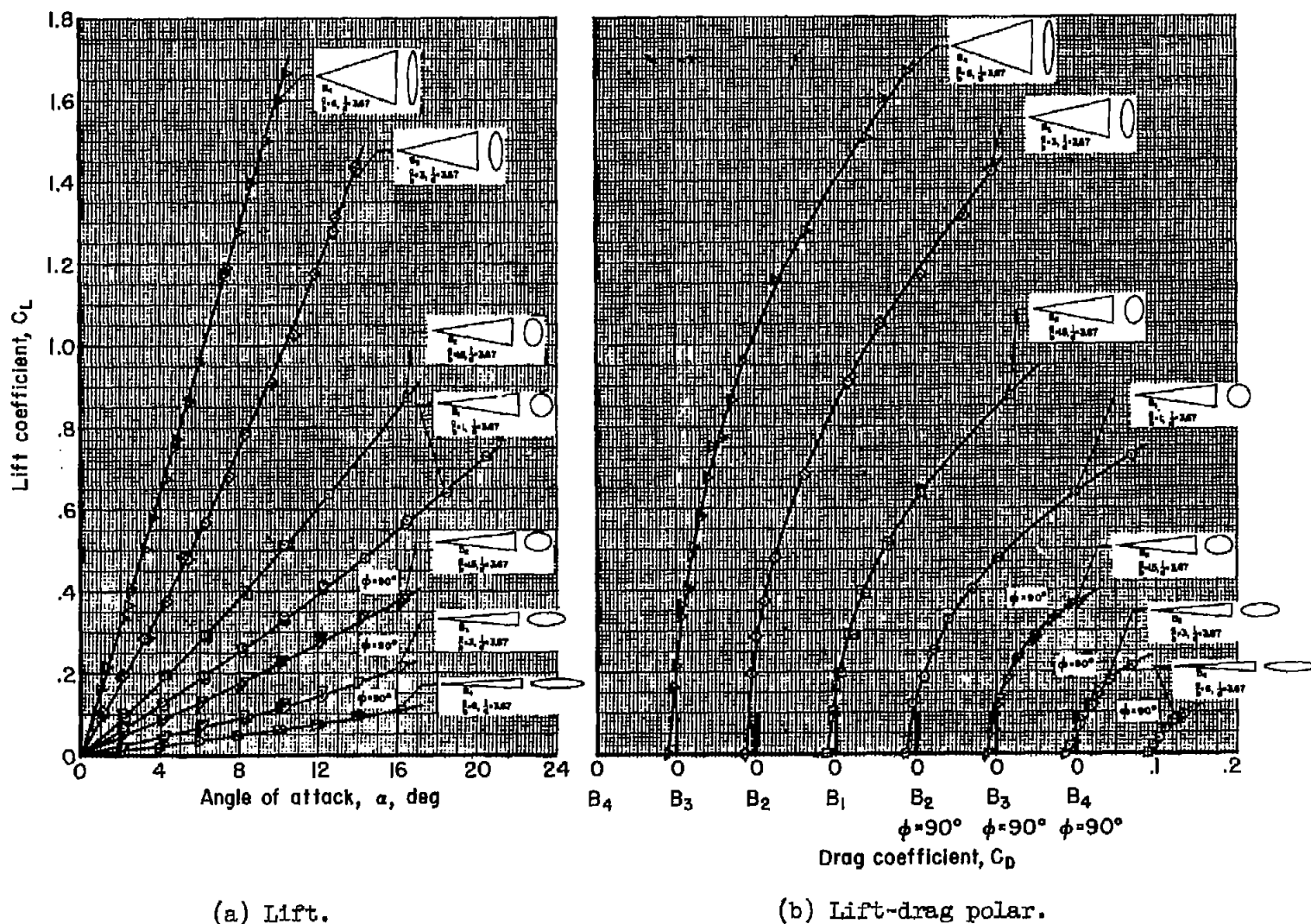
Figure 3.- Effect of change in axis ratio (a/b) on the aerodynamic characteristics of elliptic cones; l/d = 3.67, M_∞ = 1.97.

(d) Center of pressure.

(c) Lift-drag ratio.

(e) Pitching moment.

Figure 3.- Concluded.

(a) Lift.

(b) Lift-drag polar.
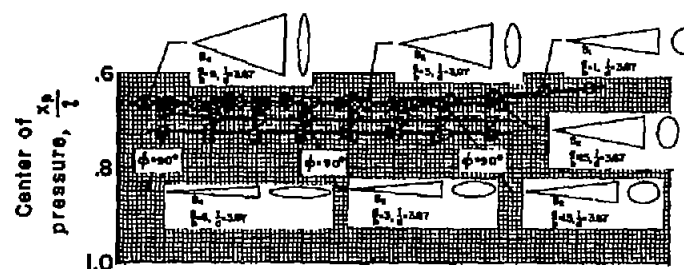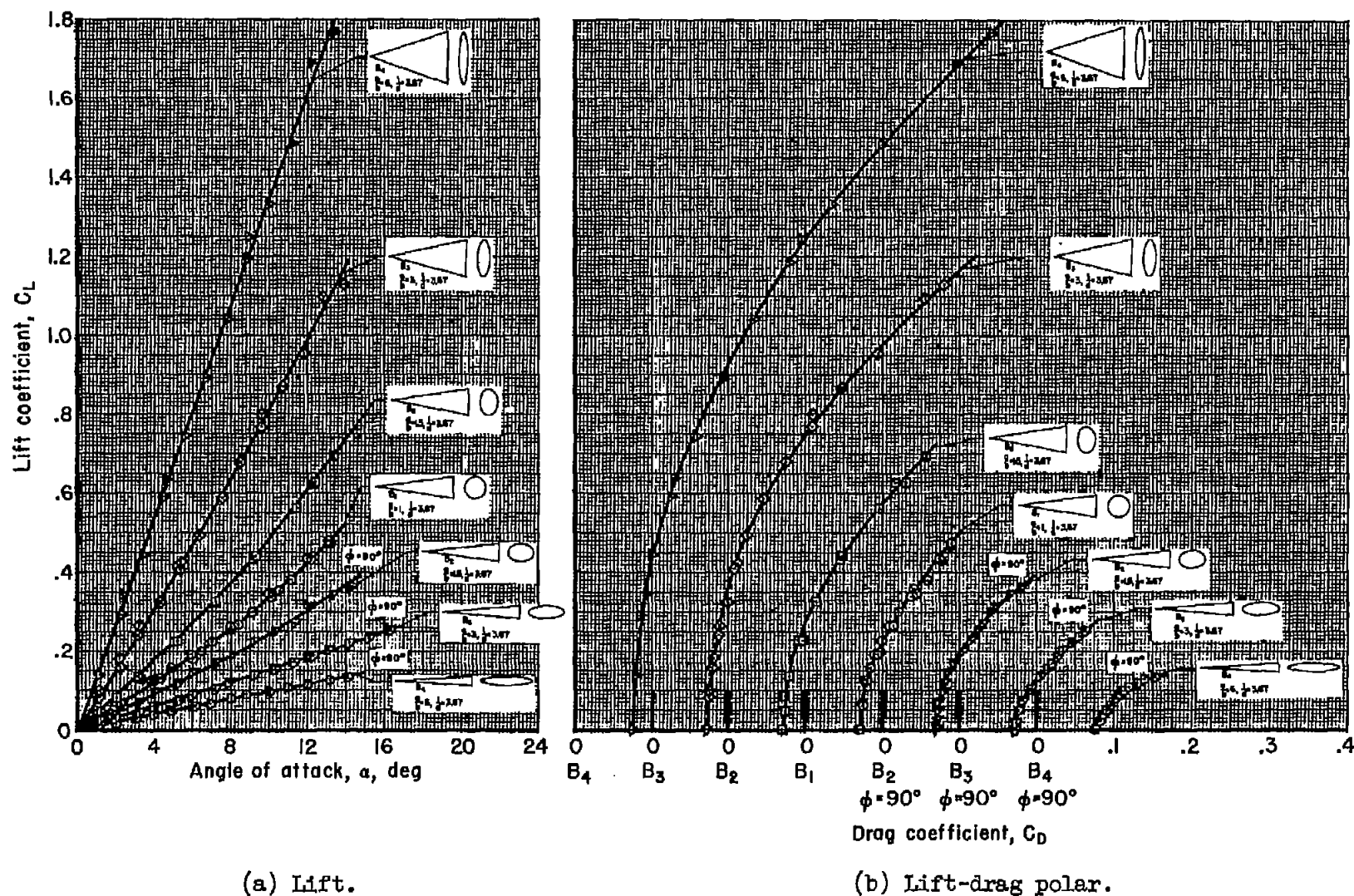
Figure 4.- Effect of change in axis ratio (a/b) on the aerodynamic characteristics of elliptic cones; l/d = 3.67, M_∞ = 2.94.
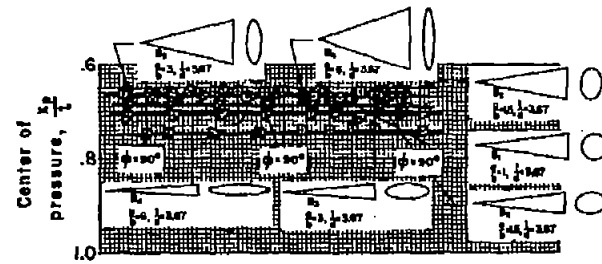
(d) Center of pressure.
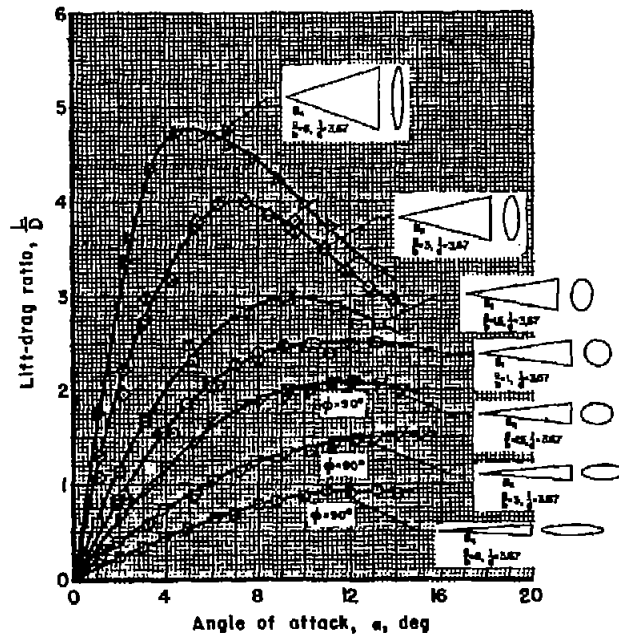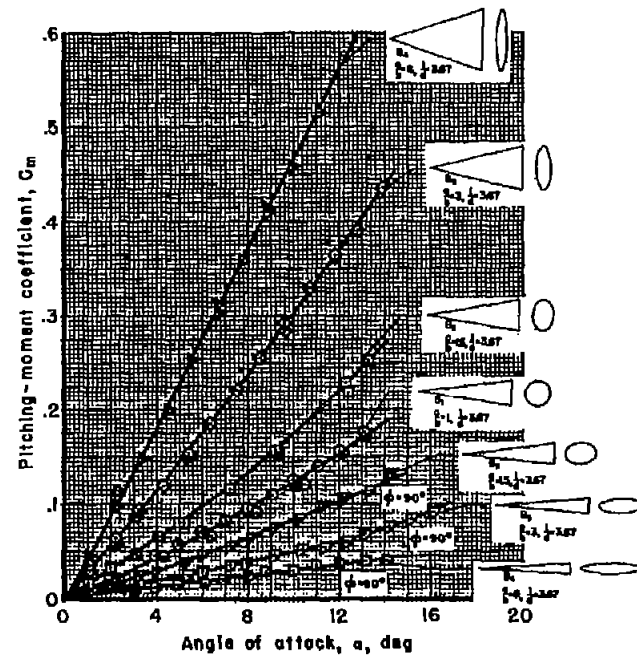
(c) Lift-drag ratio.

(e) Pitching moment.

Figure 4.- Concluded.

(a) Lift.

(b) Lift-drag polar.
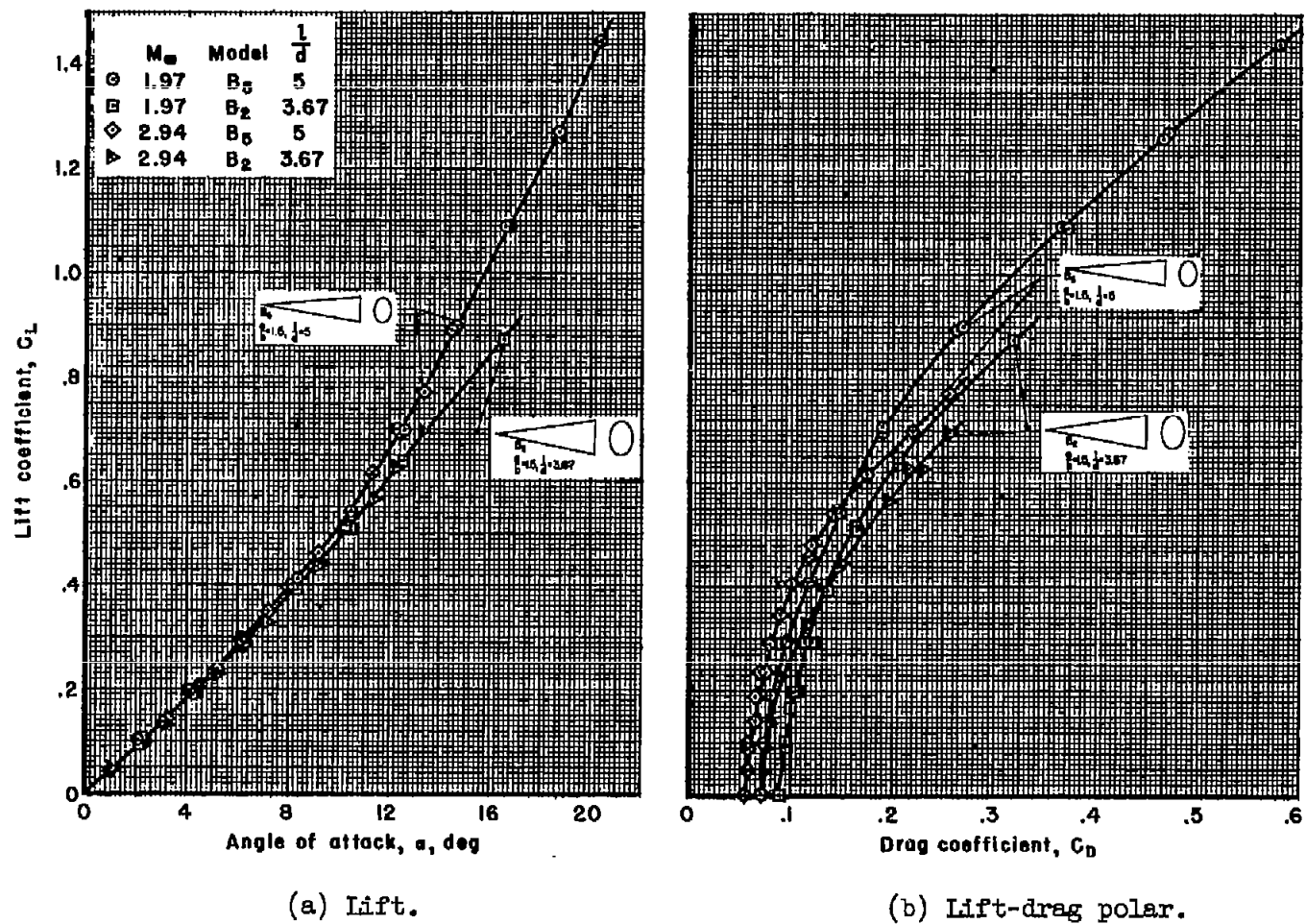
Figure 5.- Effect of change in fineness ratio on the aerodynamic characteristics of elliptic cones of a/b = 1.5.

	M_∞	Model	$\frac{l}{d}$
⊙	1.97	B_5	5
⊟	1.97	B_2	3.67
◇	2.94	B_5	5
▷	2.94	B_2	3.67
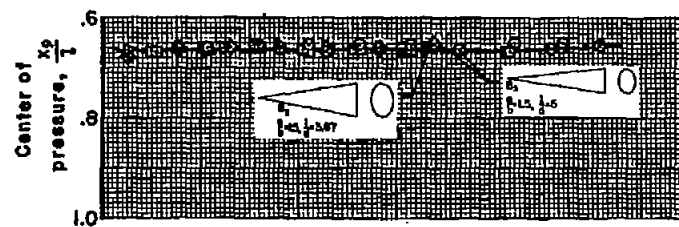
(d) Center of pressure.
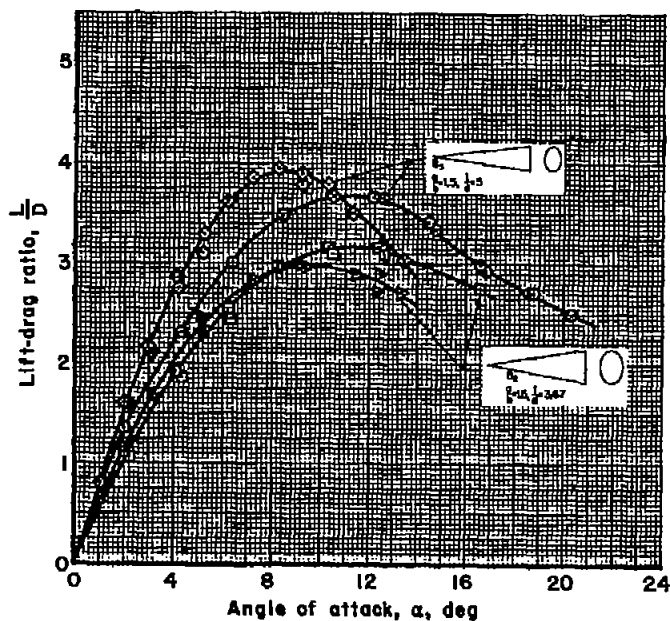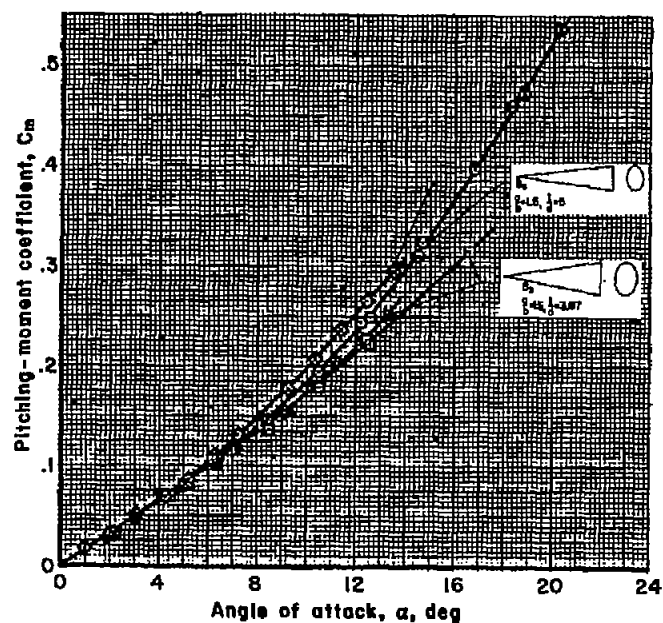
(c) Lift-drag ratio.

(e) Pitching moment.

Figure 5.- Concluded.
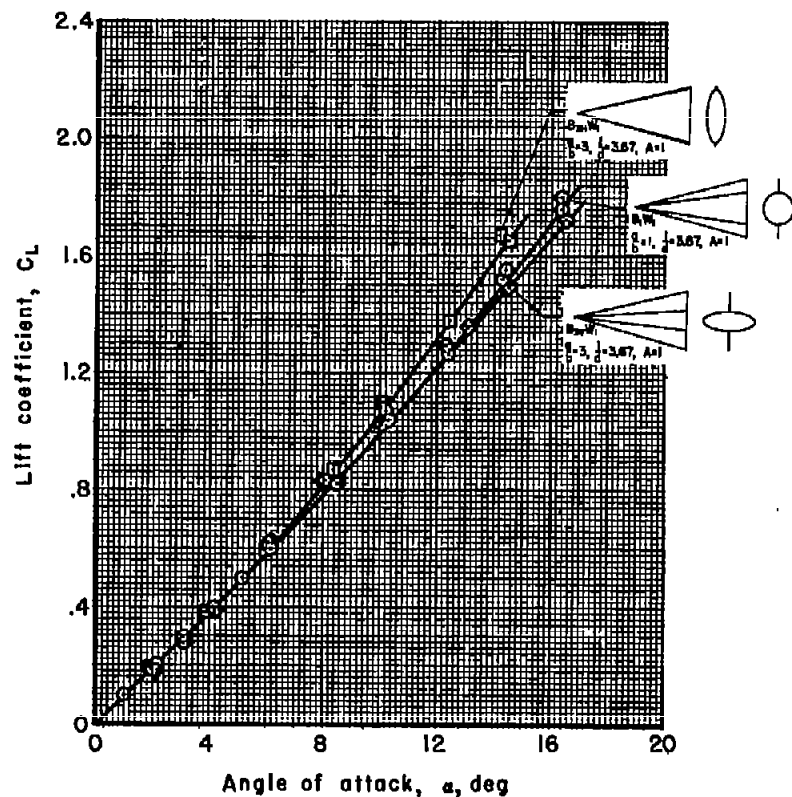
(a) Lift.
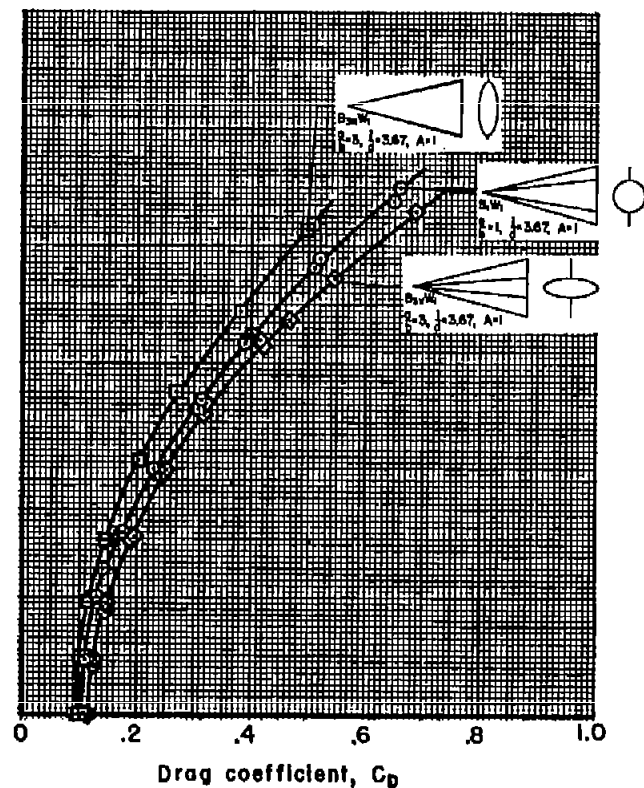
(b) Lift-drag polar.

Figure 6.- Effect of change in axis ratio (a/b) and arrangement on the aerodynamic
characteristics of elliptic cones with wings of aspect ratio 1; M_{∞} = 1.97.
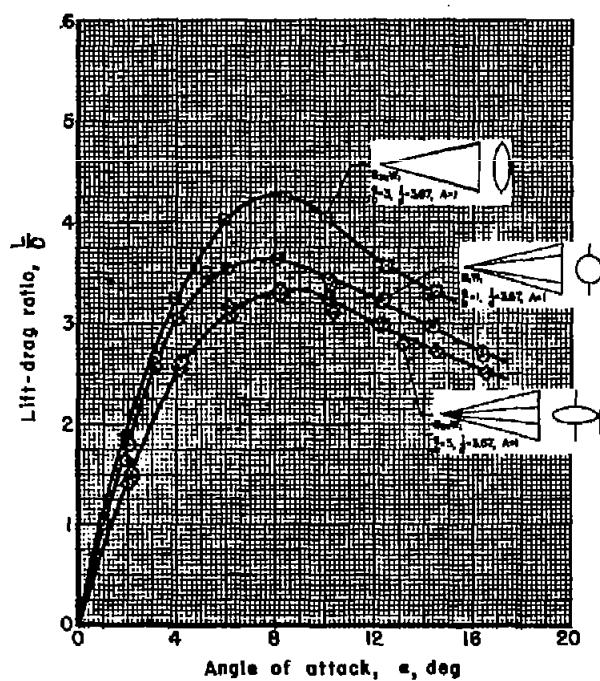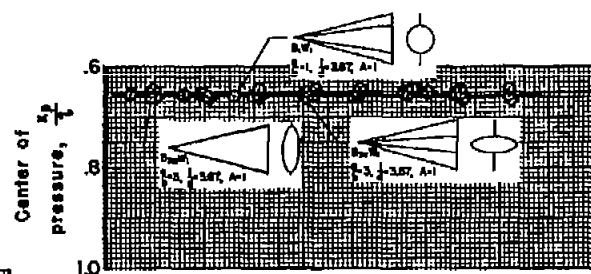
(d) Center of pressure.
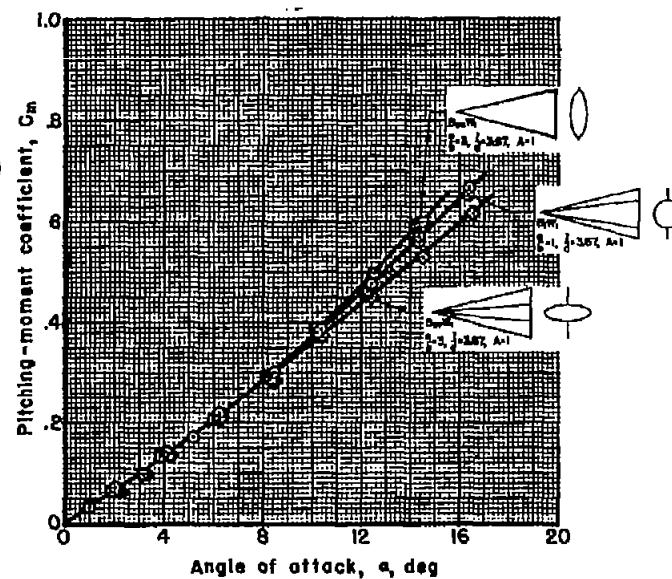
(c) Lift-drag ratio.

(e) Pitching moment.

Figure 6.- Concluded.

(a) Lift.

(b) Lift-drag polar.

Figure 7.- Effect of change in axis ratio (a/b) and arrangement on the aerodynamic characteristics of elliptic cones with wings of aspect ratio 1; $M_{\infty} = 2.94$.
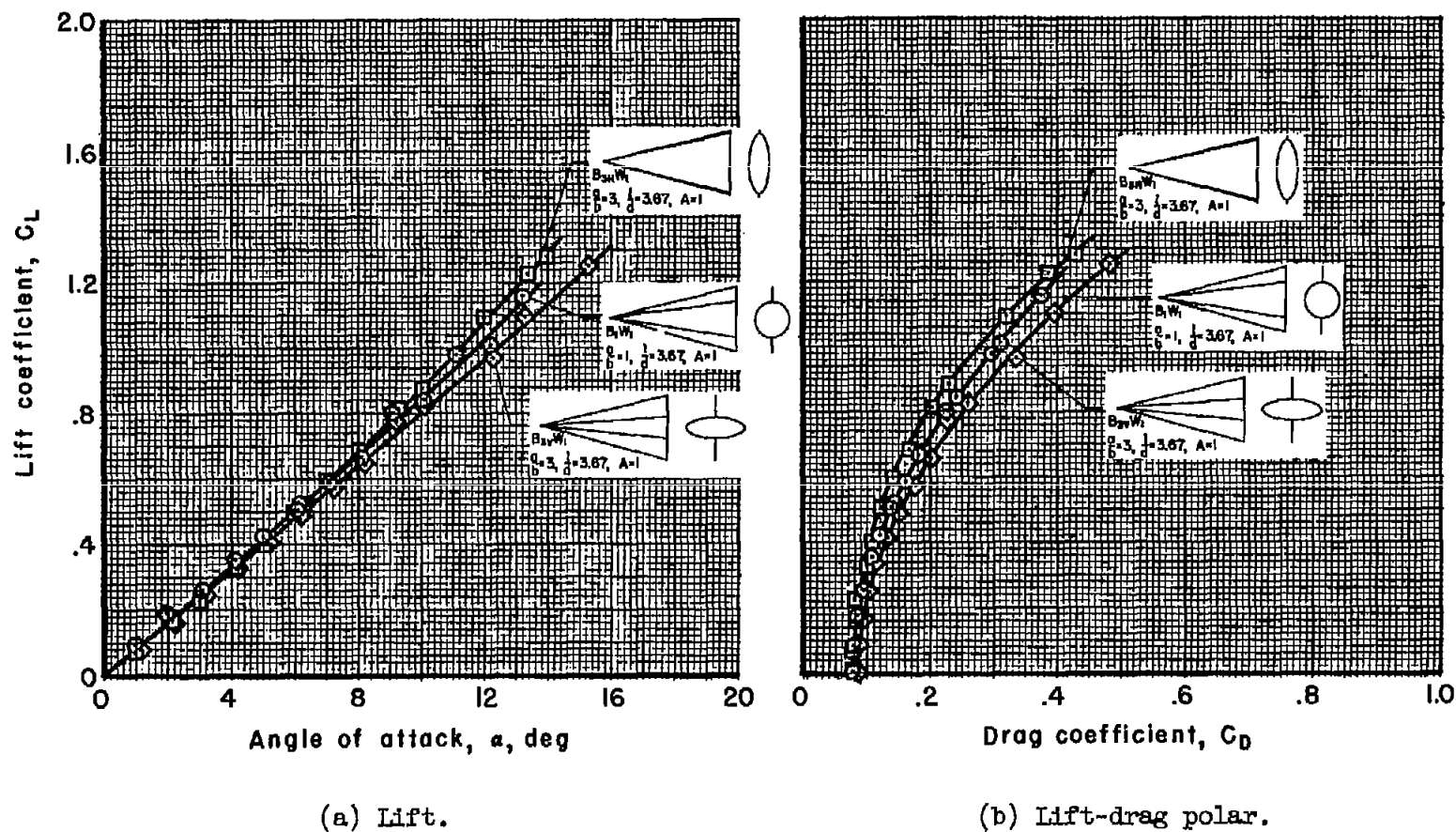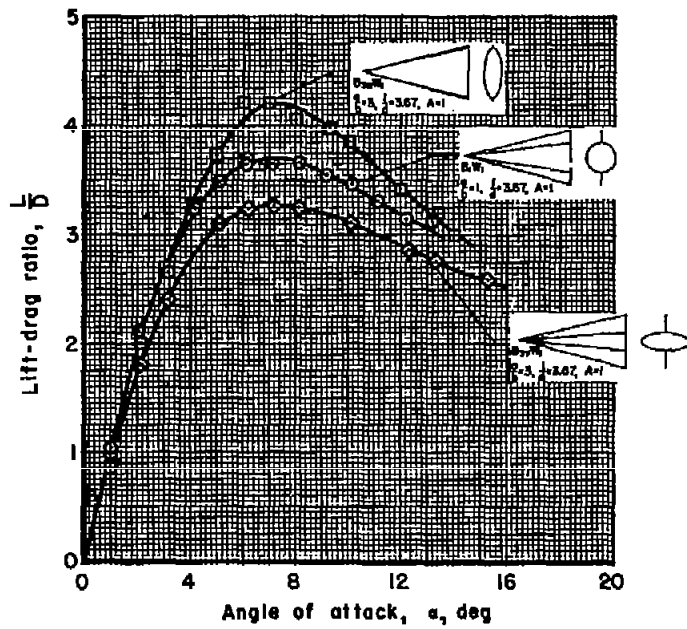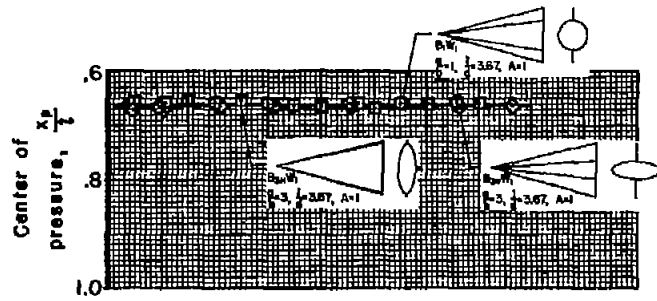
(d) Center of pressure.
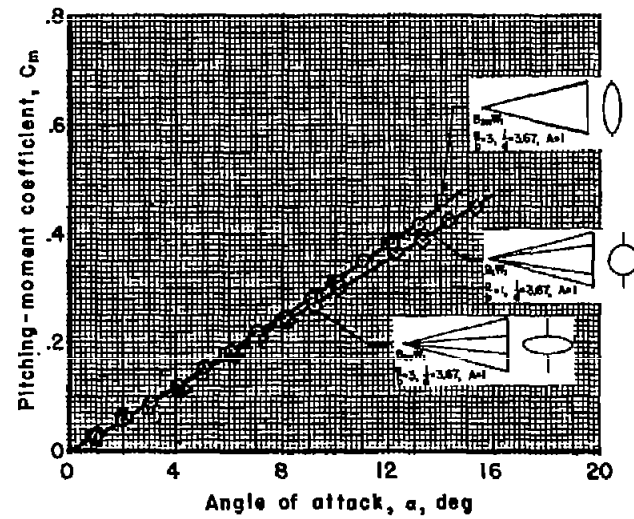
(c) Lift-drag ratio.

(e) Pitching moment.

Figure 7.- Concluded.

(a) Lift.
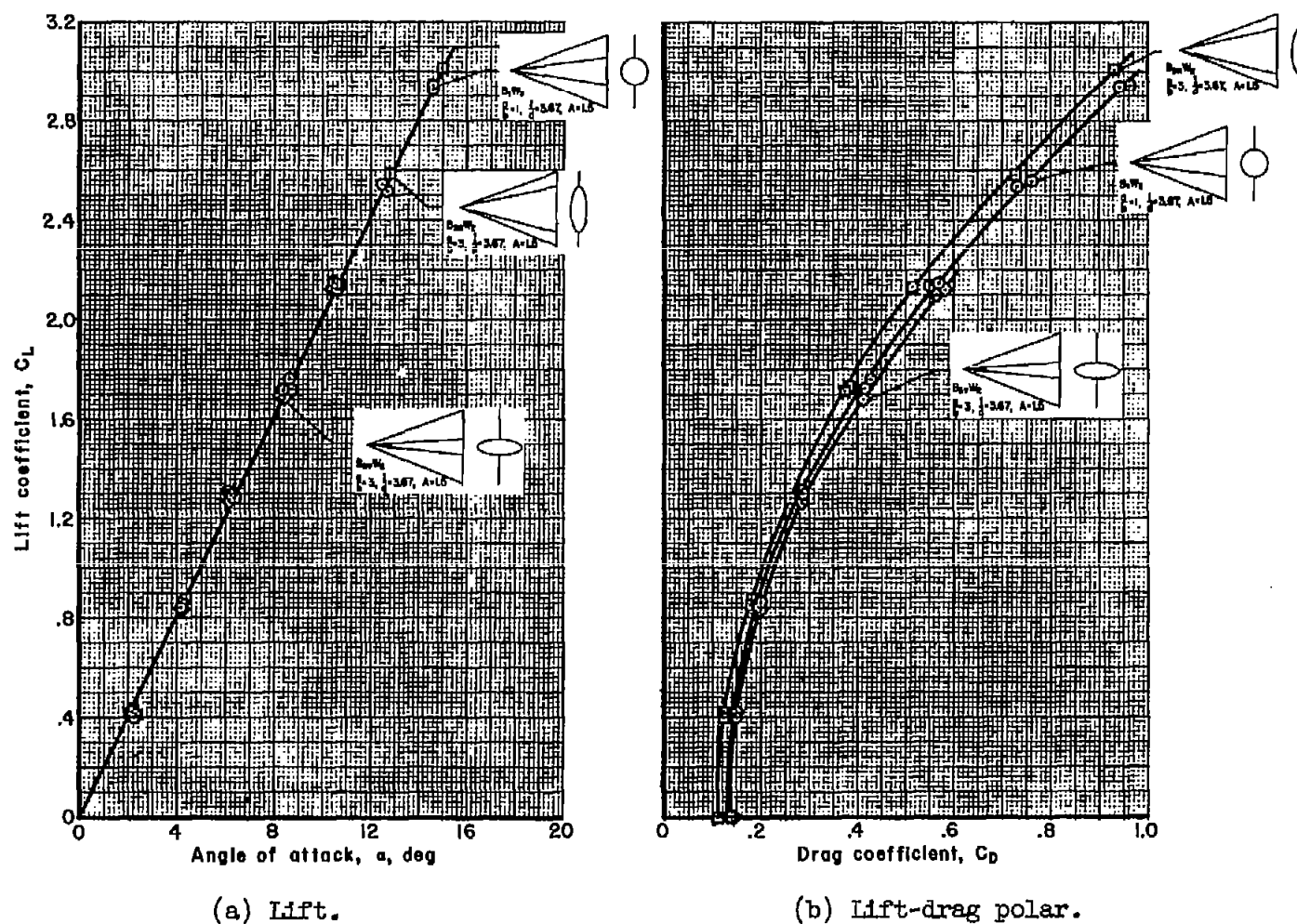
(b) Lift-drag polar.

Figure 8.- Effect of change in axis ratio (a/b) and arrangement on the aerodynamic characteristics of elliptic cones with wings of aspect ratio 1.5; $M_\infty = 1.97$.
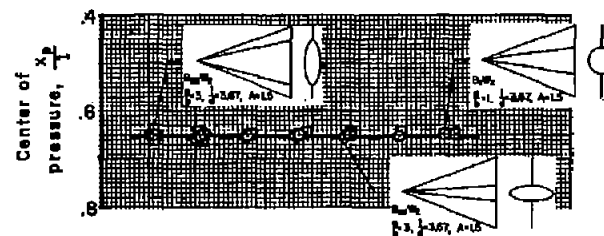
(d) Center of pressure.
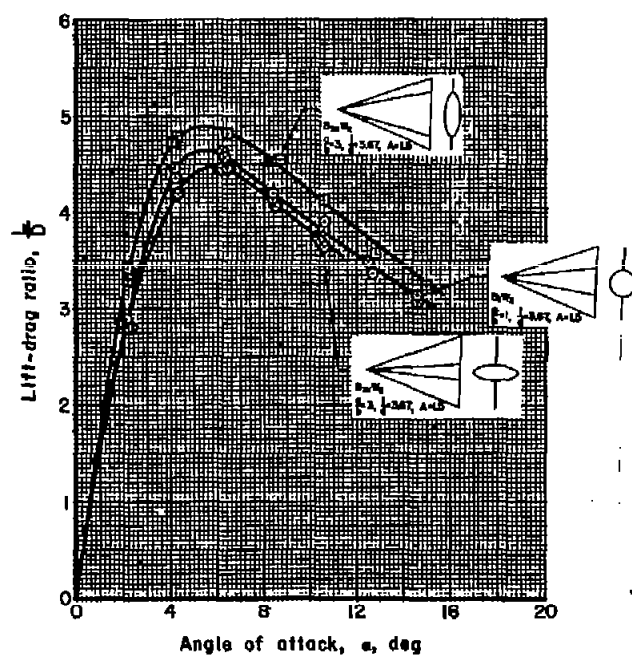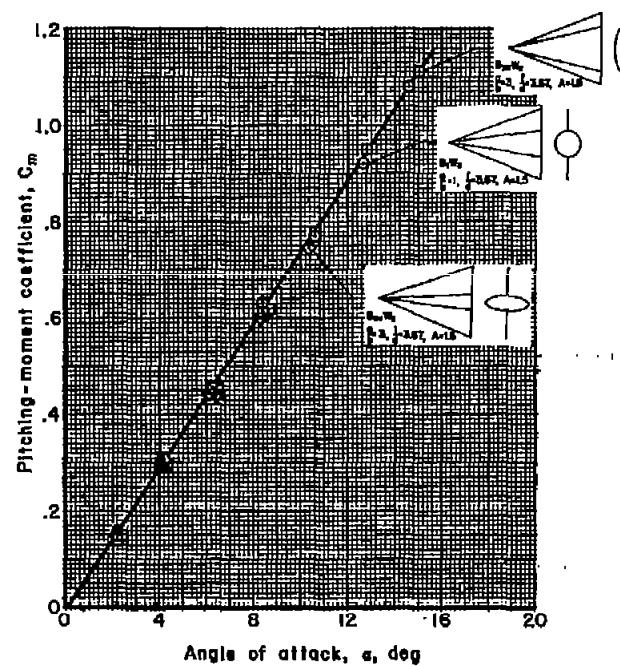
(c) Lift-drag ratio.

(e) Pitching moment.

Figure 8.- Concluded.
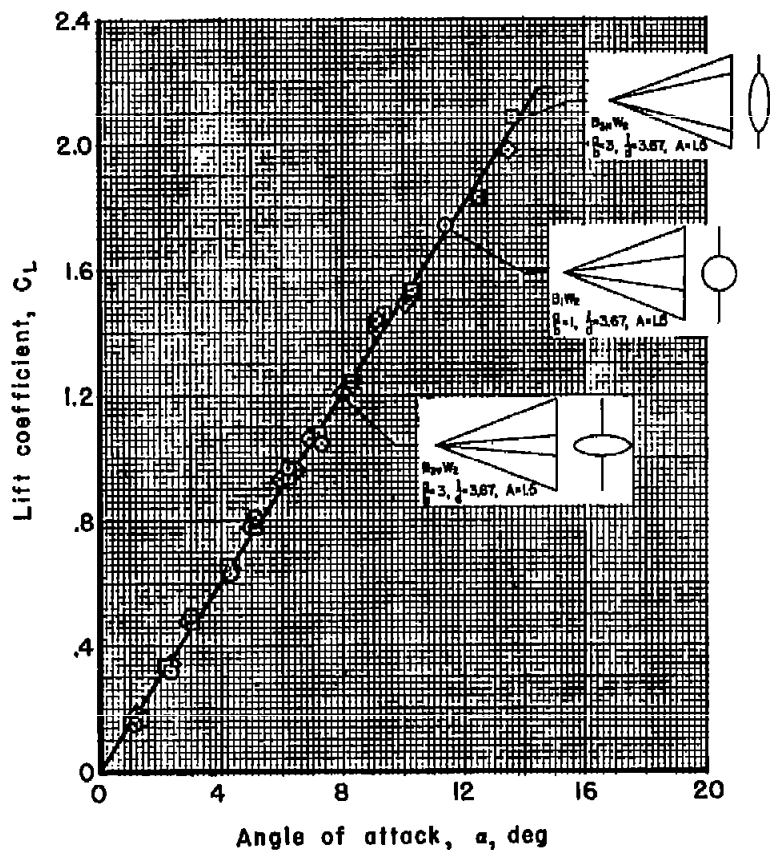
(a) Lift.
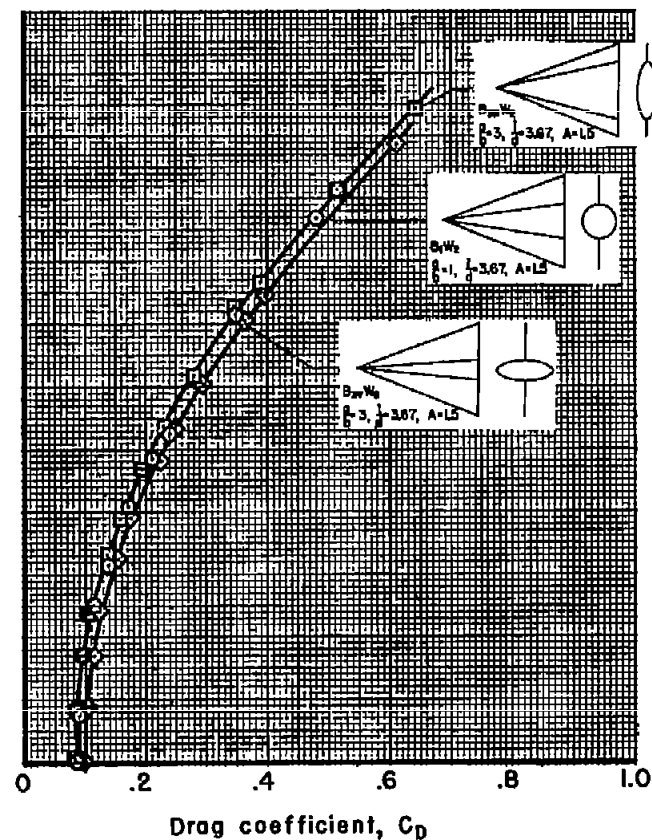
(b) Lift-drag polar.

Figure 9.- Effect of change in axis ratio (a/b) and arrangement on the aerodynamic characteristics of elliptic cones with wings of aspect ratio 1.5; $M_\infty = 2.94$.
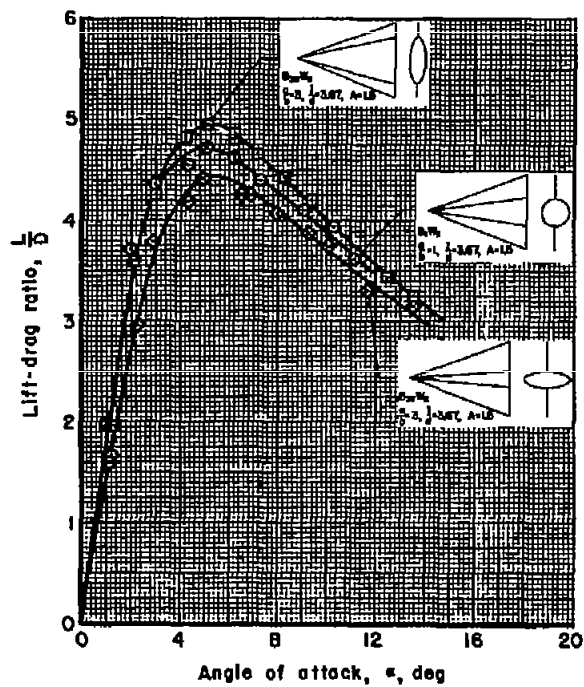
(d) Center of pressure.

(c) Lift-drag ratio.
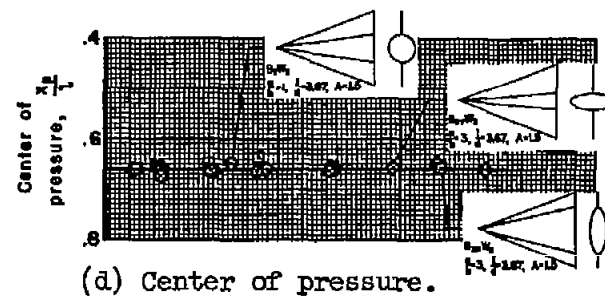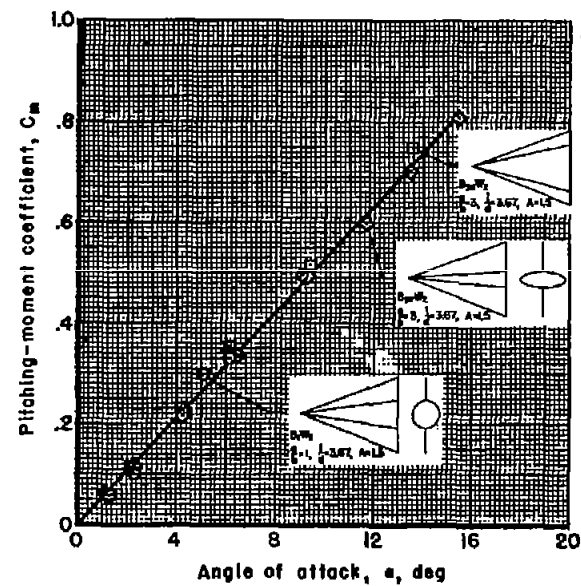
(e) Pitching moment.

Figure 9.- Concluded.
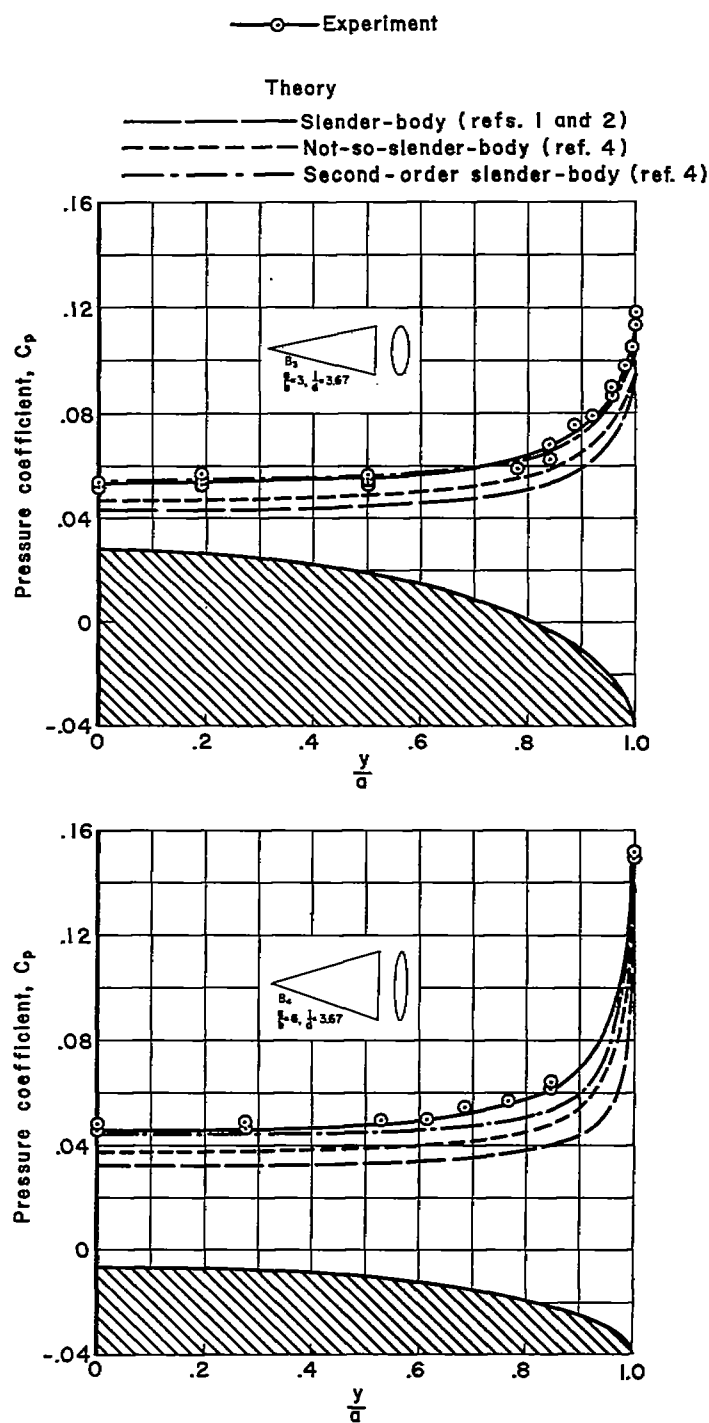
Figure 10.- Comparison of theoretical and experimental pressure distributions for elliptic cones at zero angle of attack; $M_\infty = 1.97$.

Experiment

⊙ From force measurements
⊡ From pressure distributions

Theory
⟩ Taylor-Maccoll circular cone (ref. 13)
✕ Taylor-Maccoll circular cone (ref. 13)+ turbulent
    skin friction (ref. 12)
——— Second-order slender-body (ref. 4)
——·— Second-order slender-body (ref. 4)+ turbulent
    skin friction (ref. 12)
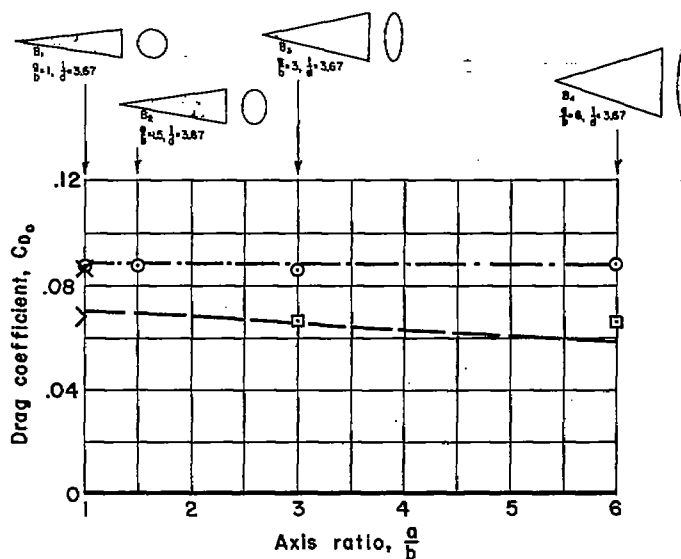
(a) $M_\infty = 1.97$.
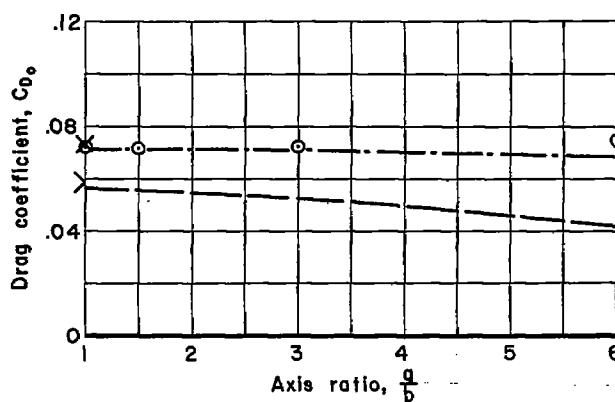
(b) $M_\infty = 2.94$

Figure 11.- Effect of change in axis ratio (a/b) on the zero-lift drag
of elliptic cones.
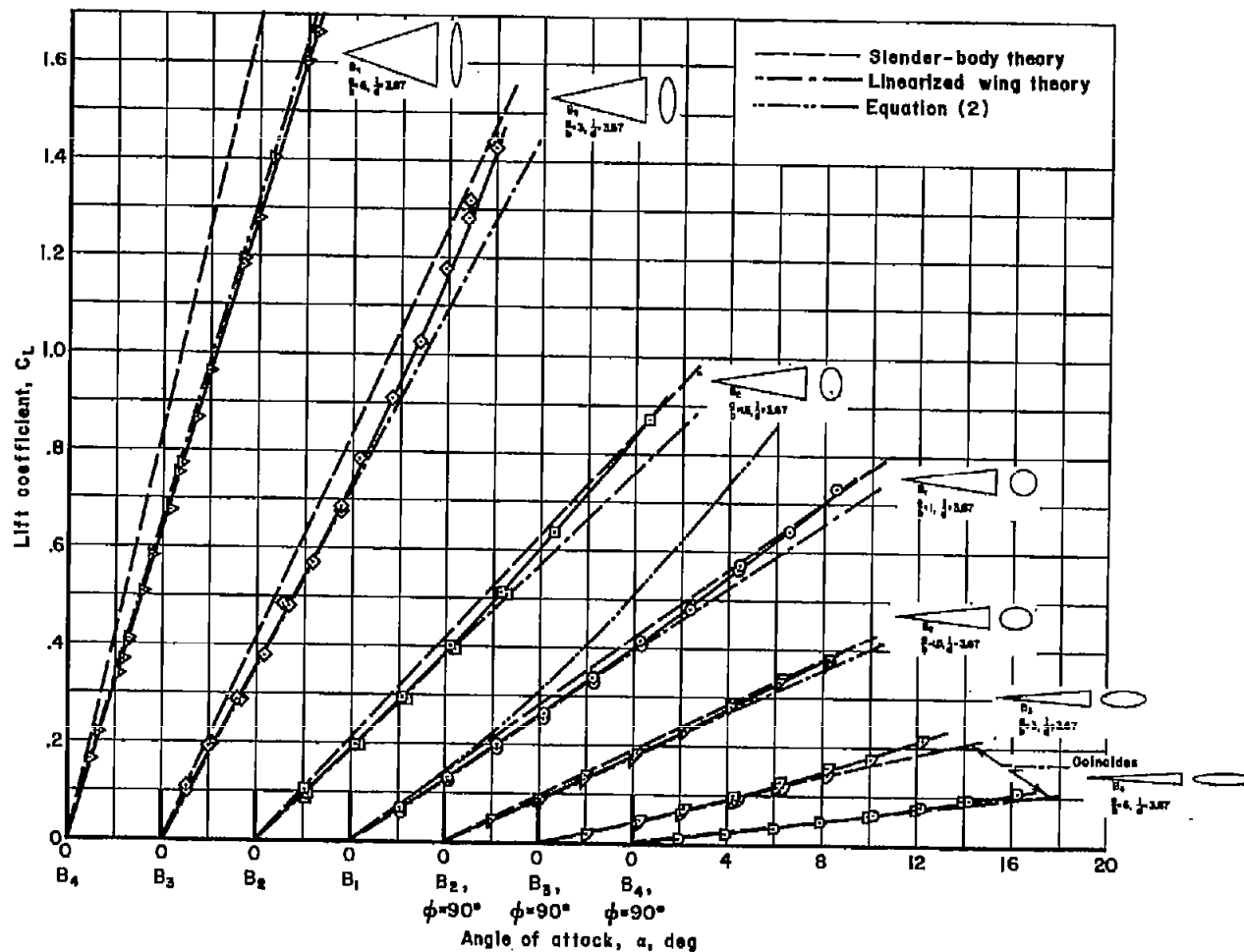
(a) Lift.

Figure 12.- Comparison of theoretical and experimental aerodynamic characteristics of elliptic cones; $l/d = 3.67$, $M_\infty = 1.97$.
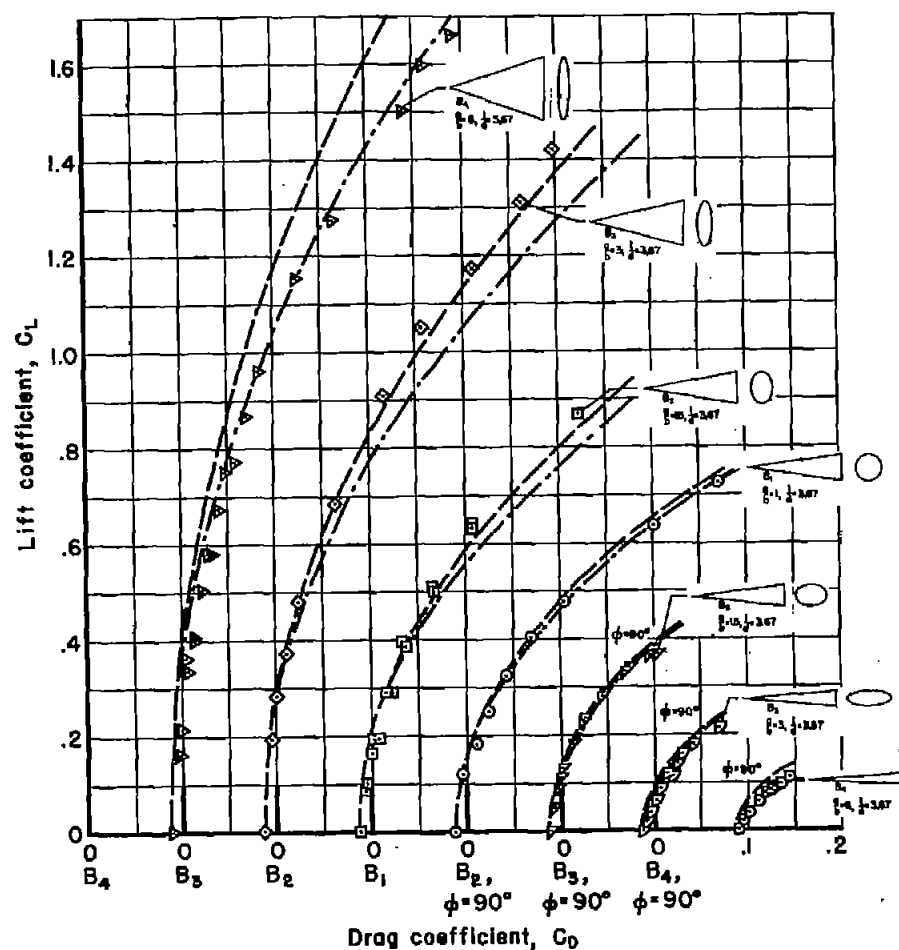
(b) Lift-drag polar.
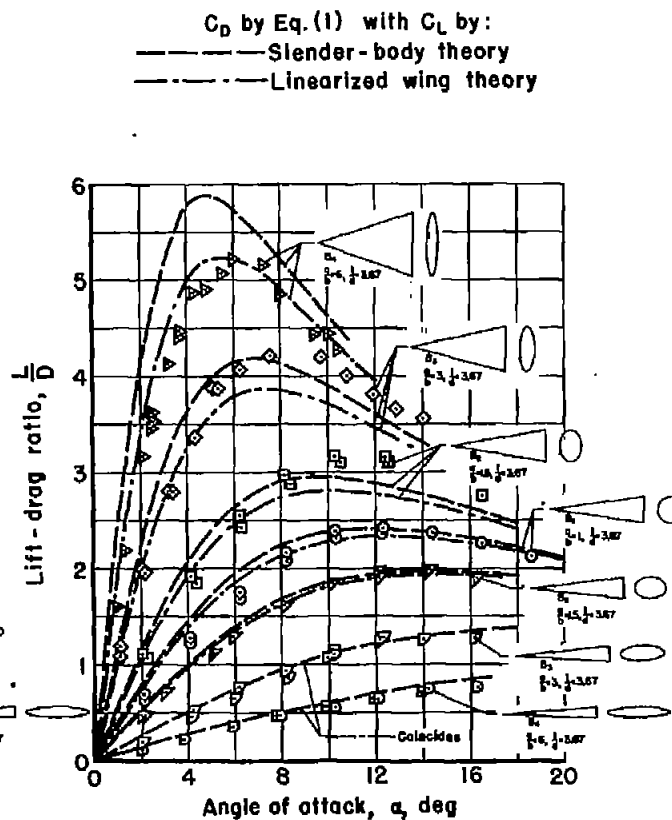
(c) Lift-drag ratio.

Figure 12.- Continued.

(d) Pitching moment.

Figure 12.- Concluded.
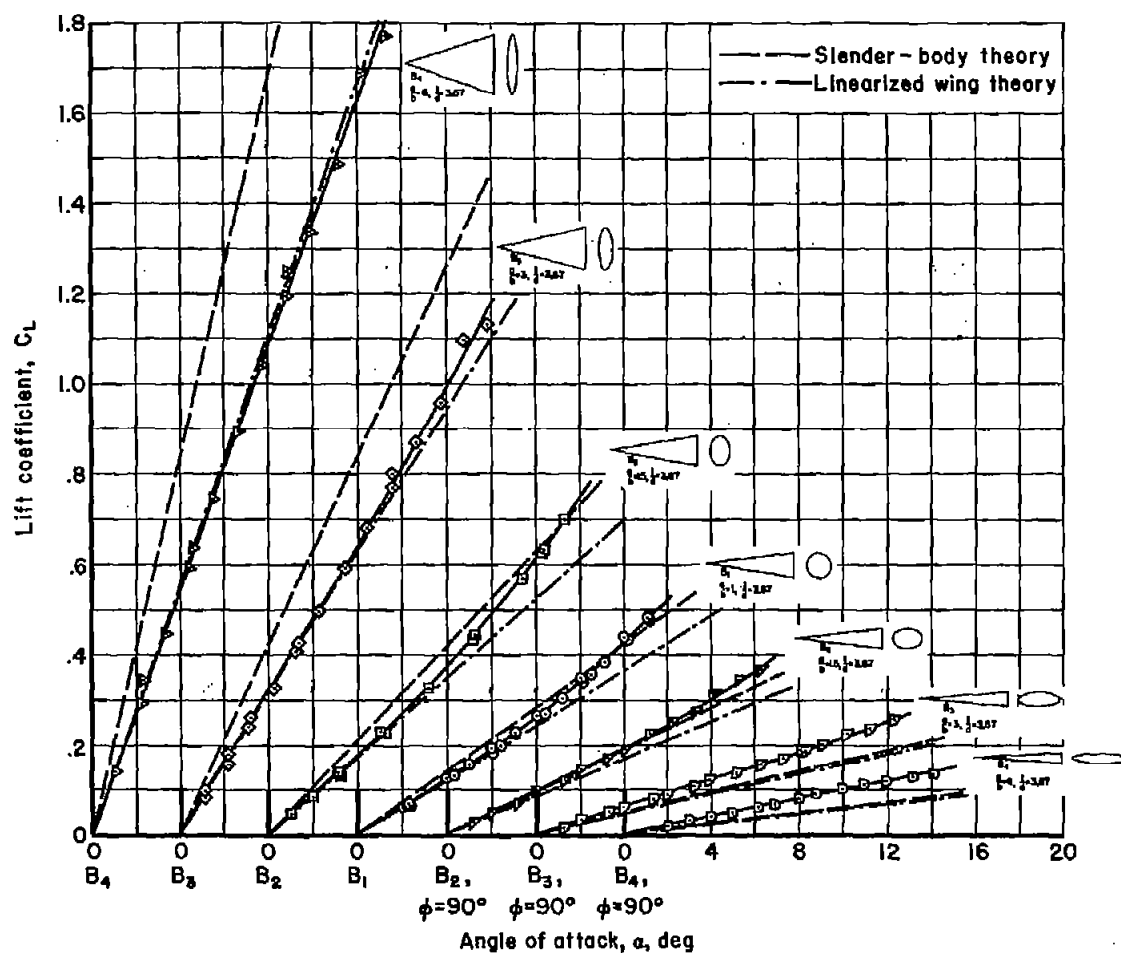
(a) Lift.

Figure 13.- Comparison of theoretical and experimental aerodynamic characteristics of elliptic cones; $l/d = 3.67$, $M_\infty = 2.94$.
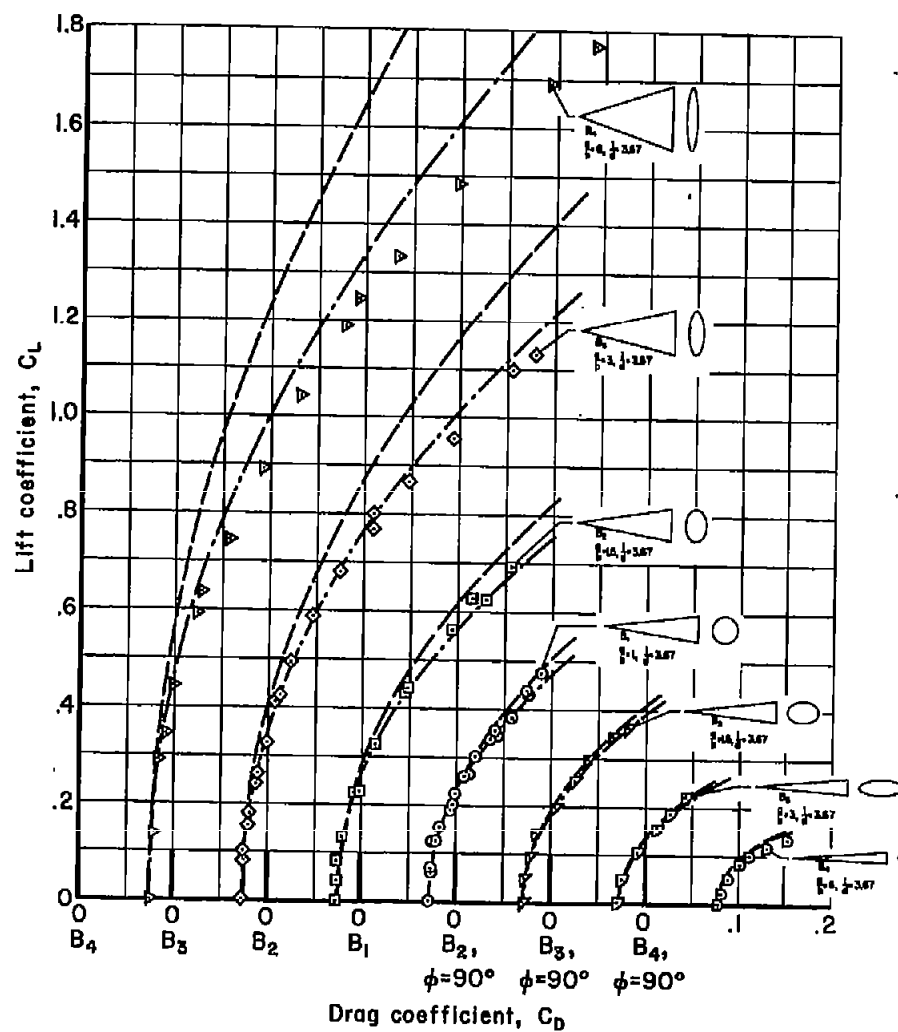
(b) Lift-drag polar.
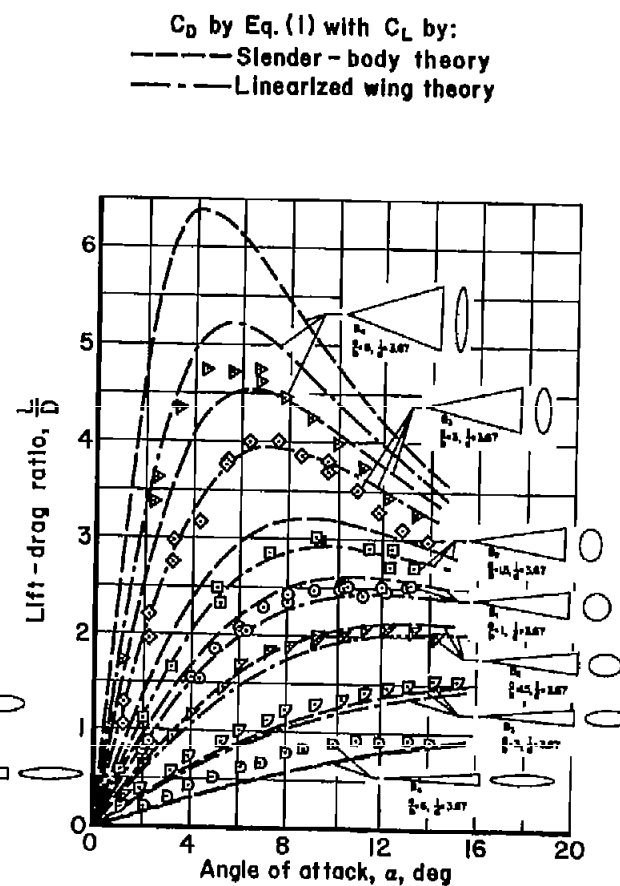
(c) Lift-drag ratio.

Figure 13.- Continued.
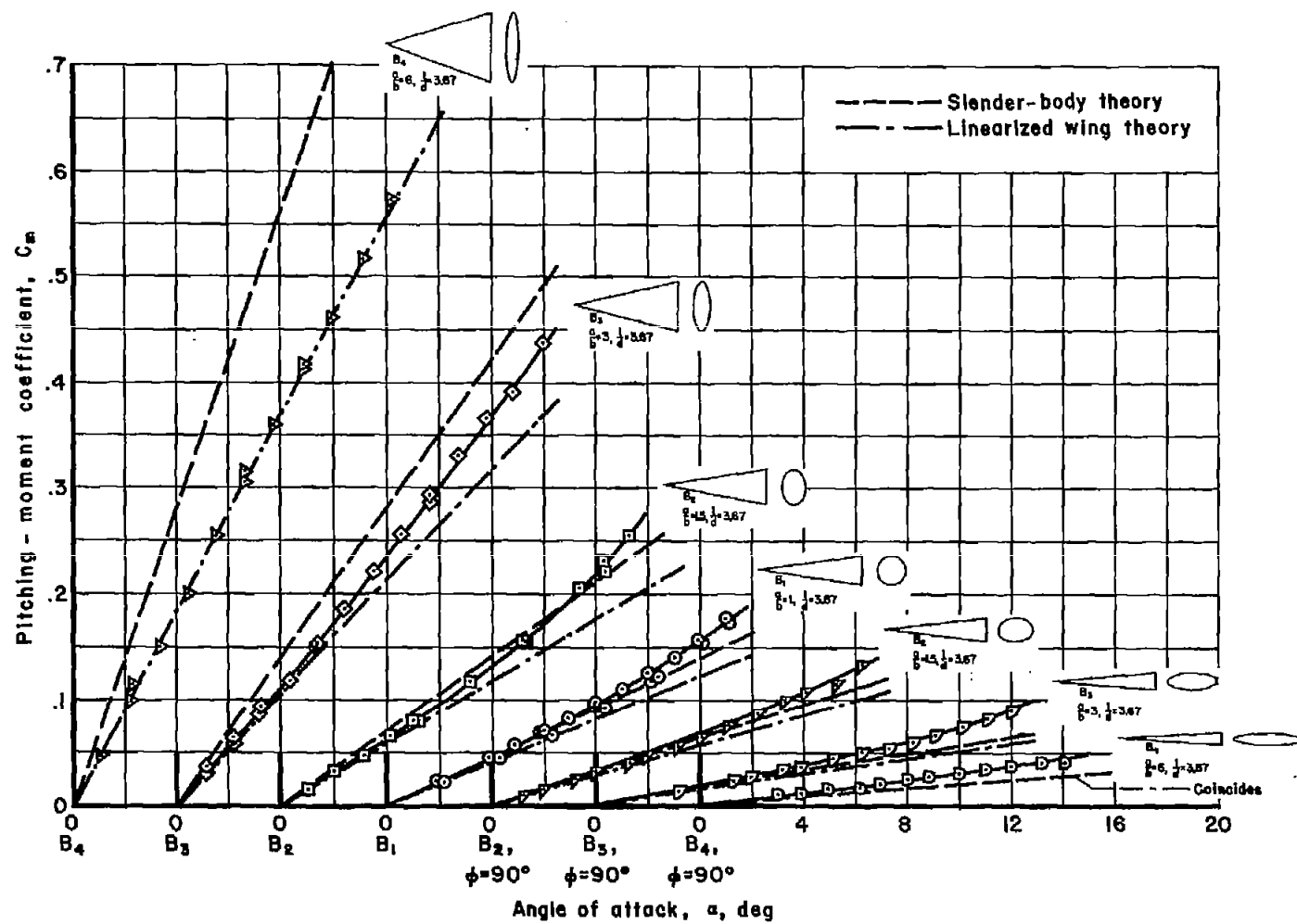
(d) Pitching moment.

Figure 13.- Concluded.
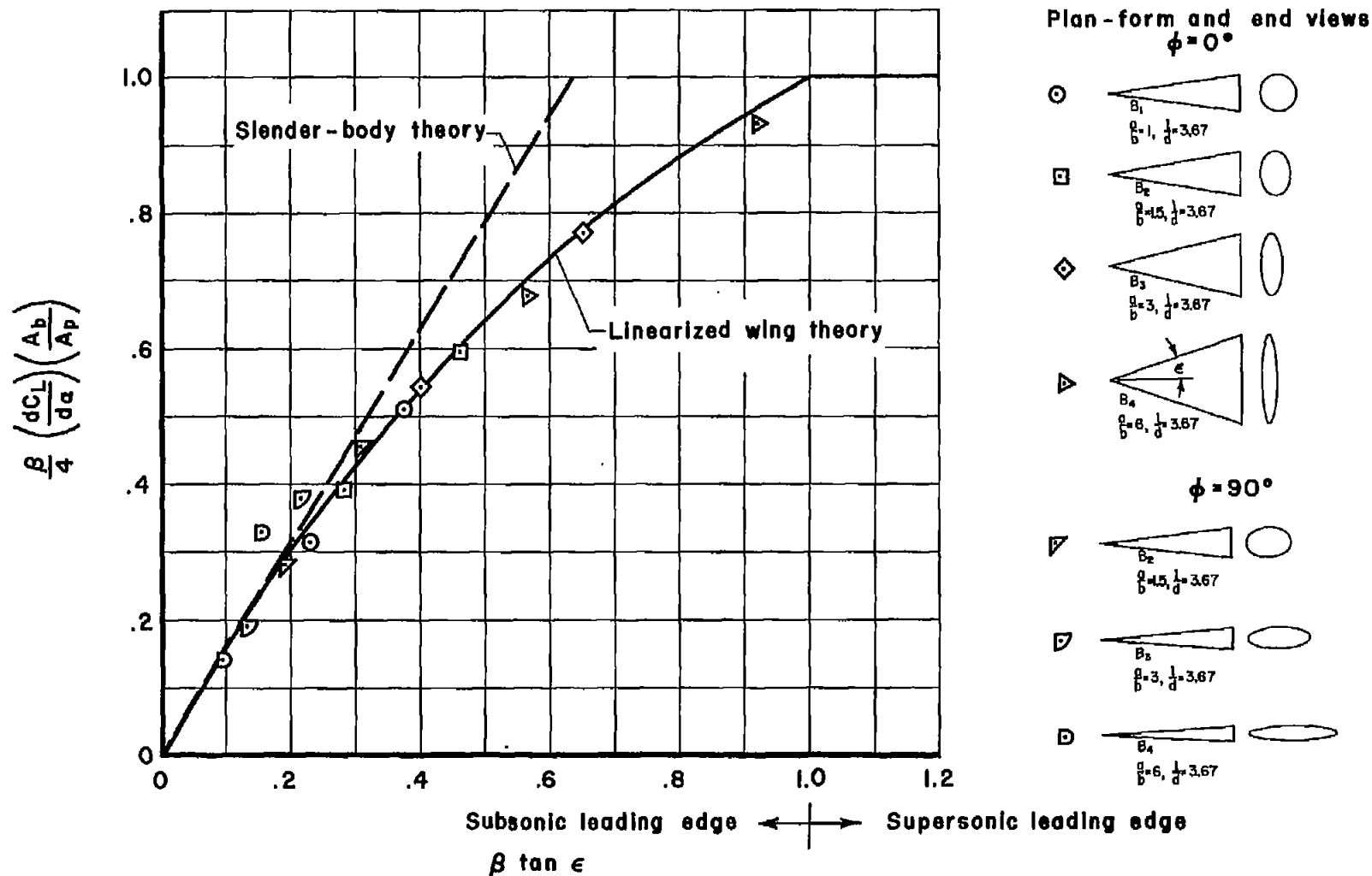
Figure 14.- Comparison of theoretical and experimental lift-curve slopes for elliptic cones at Mach numbers 1.97 and 2.94.
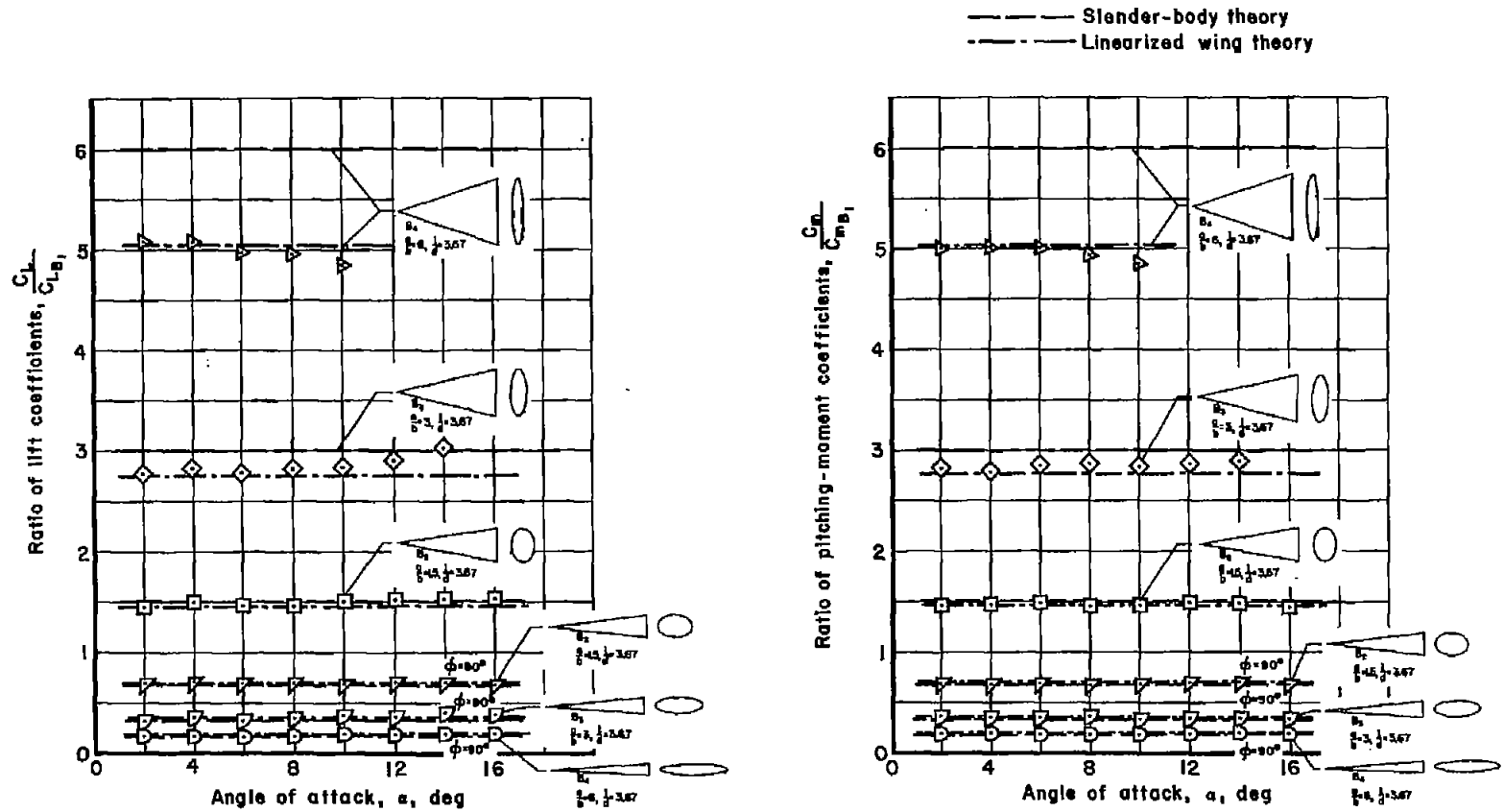
(a) $M_\infty = 1.97$

Figure 15.- Correlation of lift and pitching-moment data for elliptic cones.
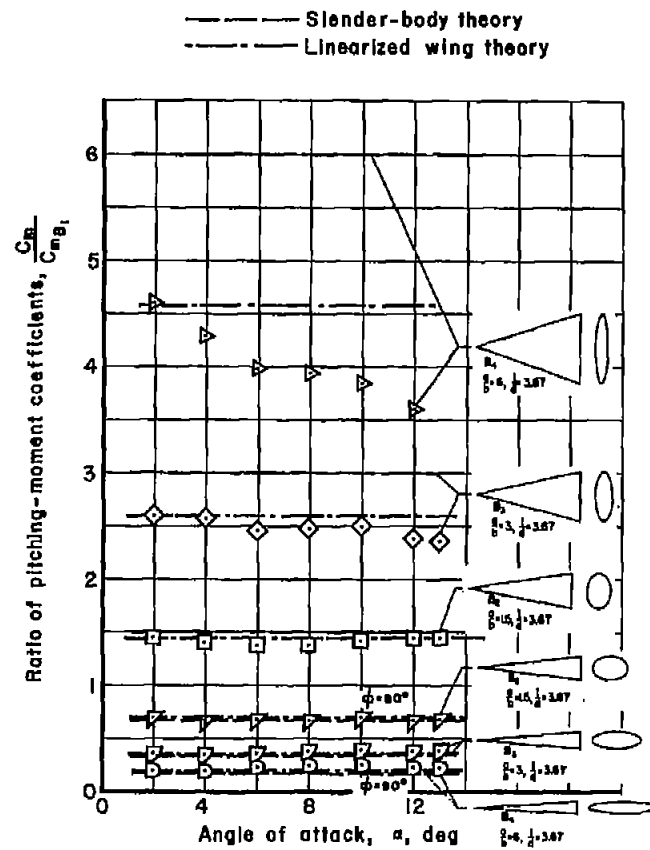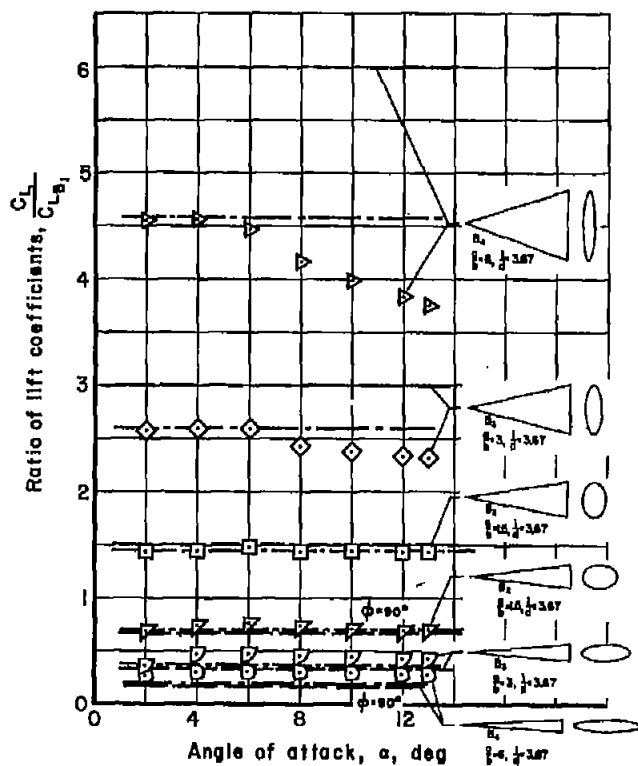
(b) $M_\infty = 2.94$

Figure 15.- Concluded.
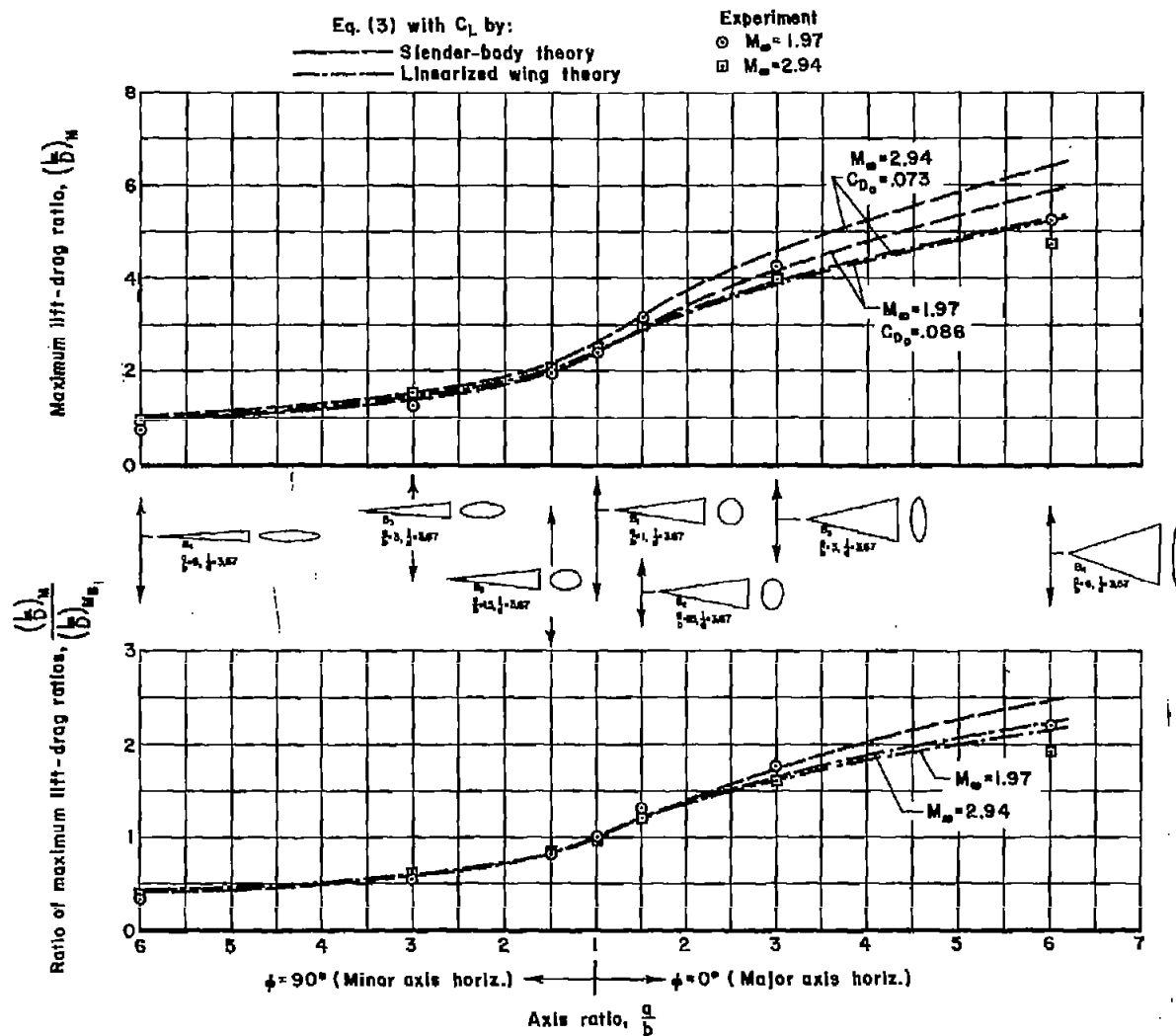
Figure 16.- Effect of axis ratio (a/b) on maximum lift-drag ratios of elliptic cones.
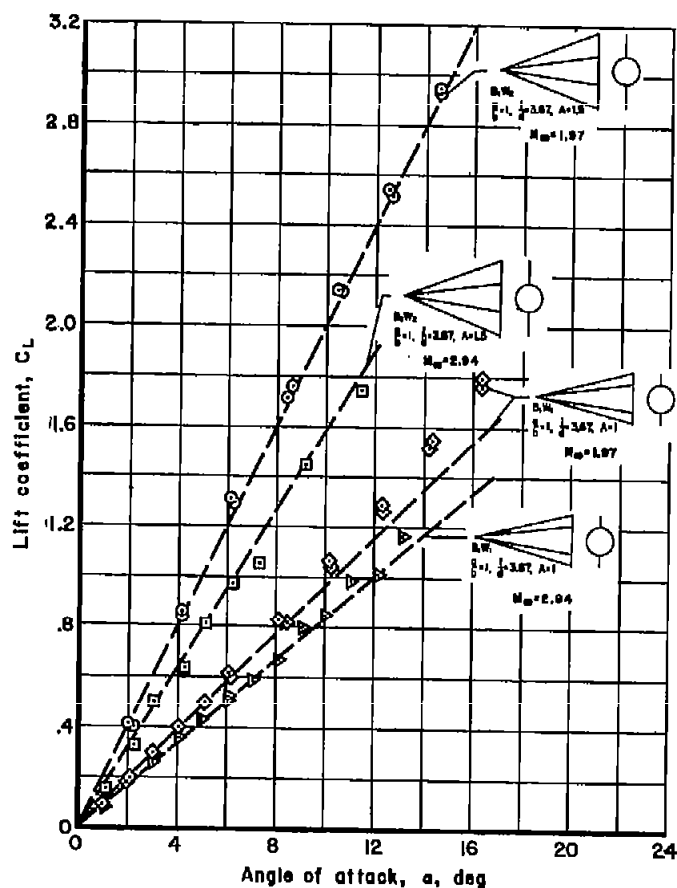
(a) Lift.
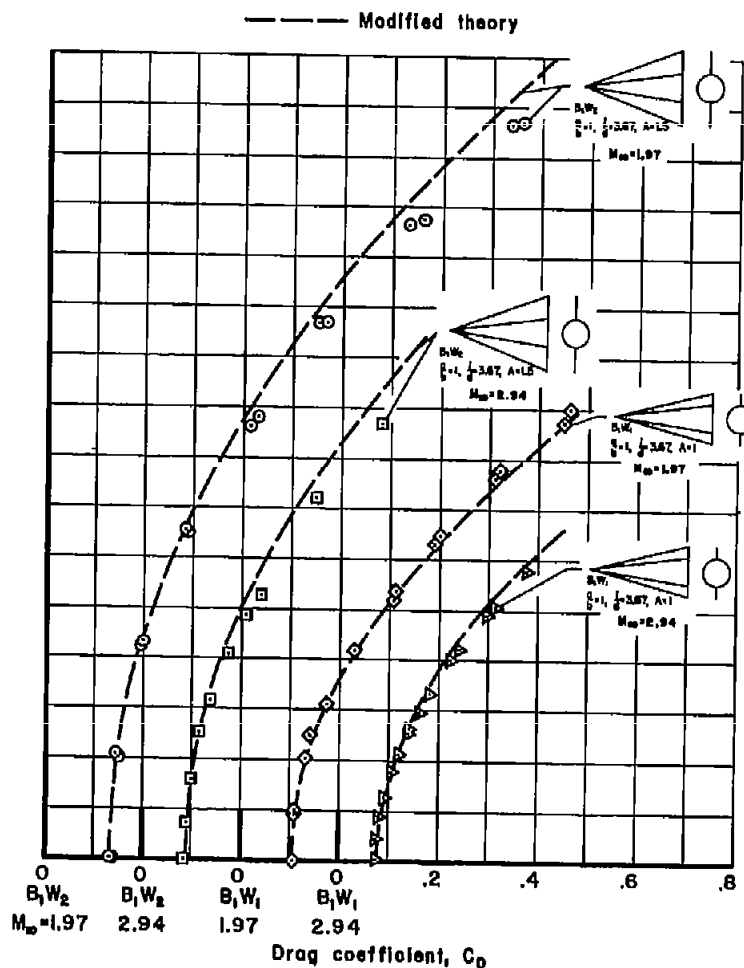
(b) Lift-drag polar.

Figure 17.- Comparison of theoretical and experimental aerodynamic characteristics of winged circular cones.

————— Modified theory
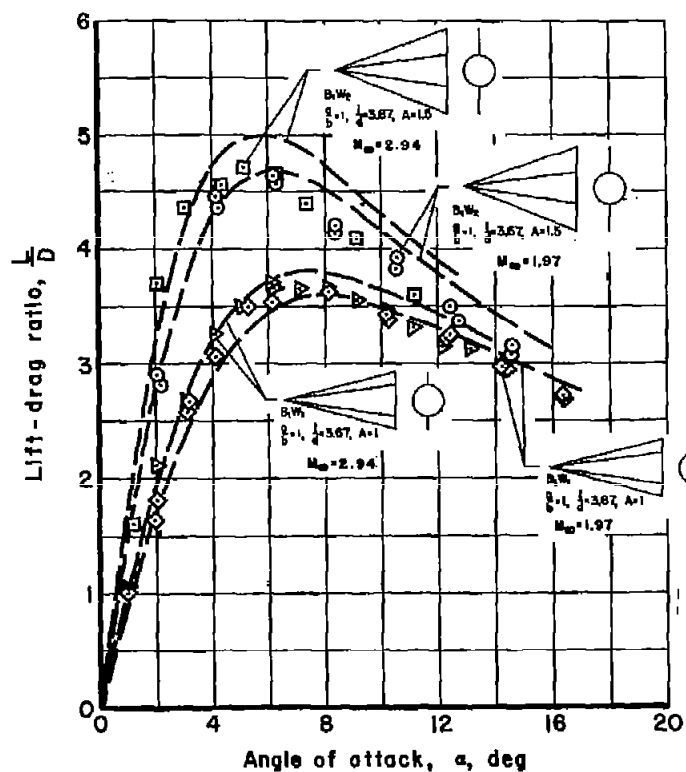
(c) Lift-drag ratio.
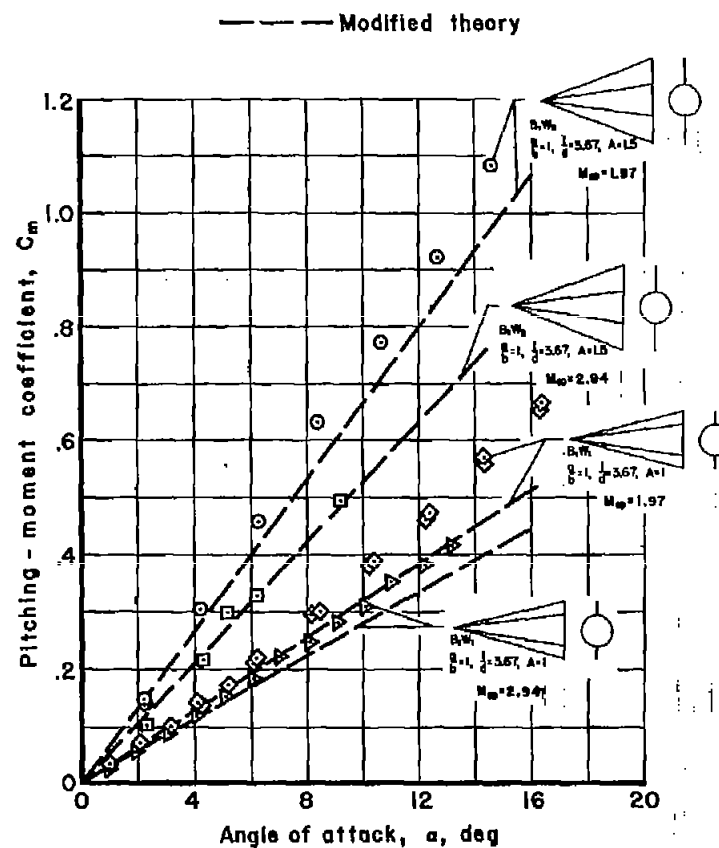
(d) Pitching moment.

Figure 17.- Concluded.
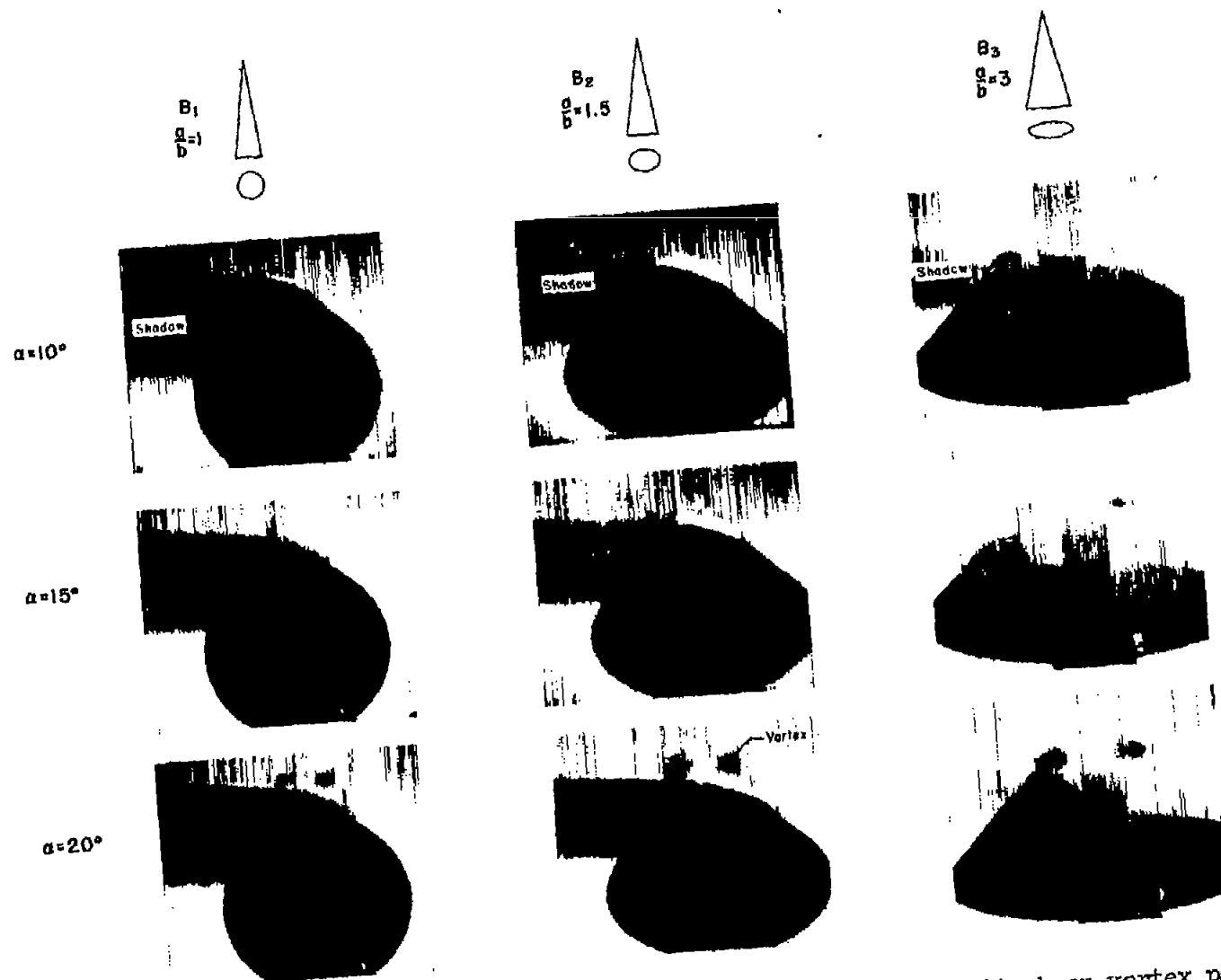
Figure 18.- Rear views of elliptic cones showing effect of angle of attack on vortex patterns (with vapor-screen light plane at $x = 0.7l$); $M_\infty = 1.97$.
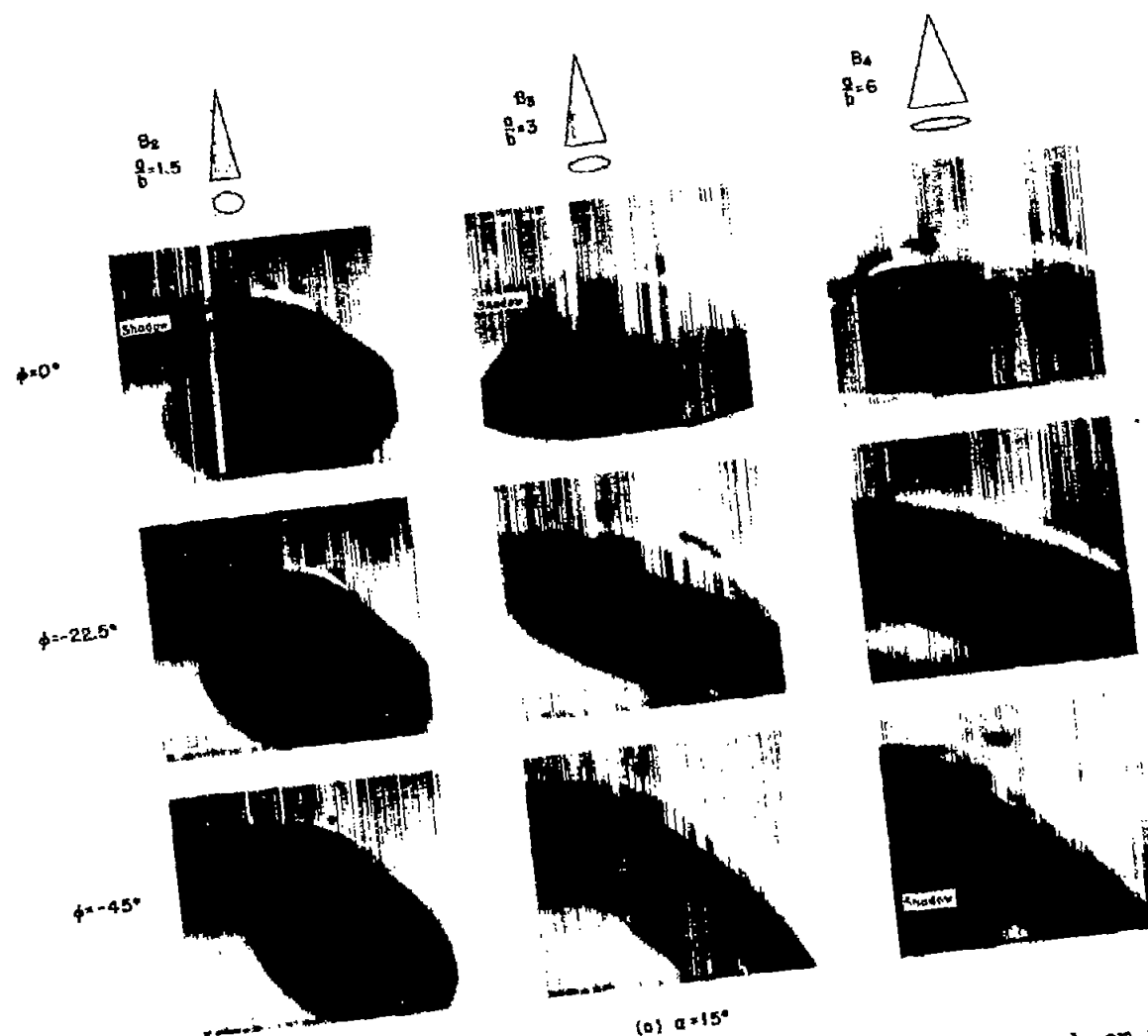
Figure 19.- Rear views of elliptic cones showing effect of angle of bank on vortex patterns (with vapor-screen light plane at $x = 0.7l$); $M_\infty = 1.97$.
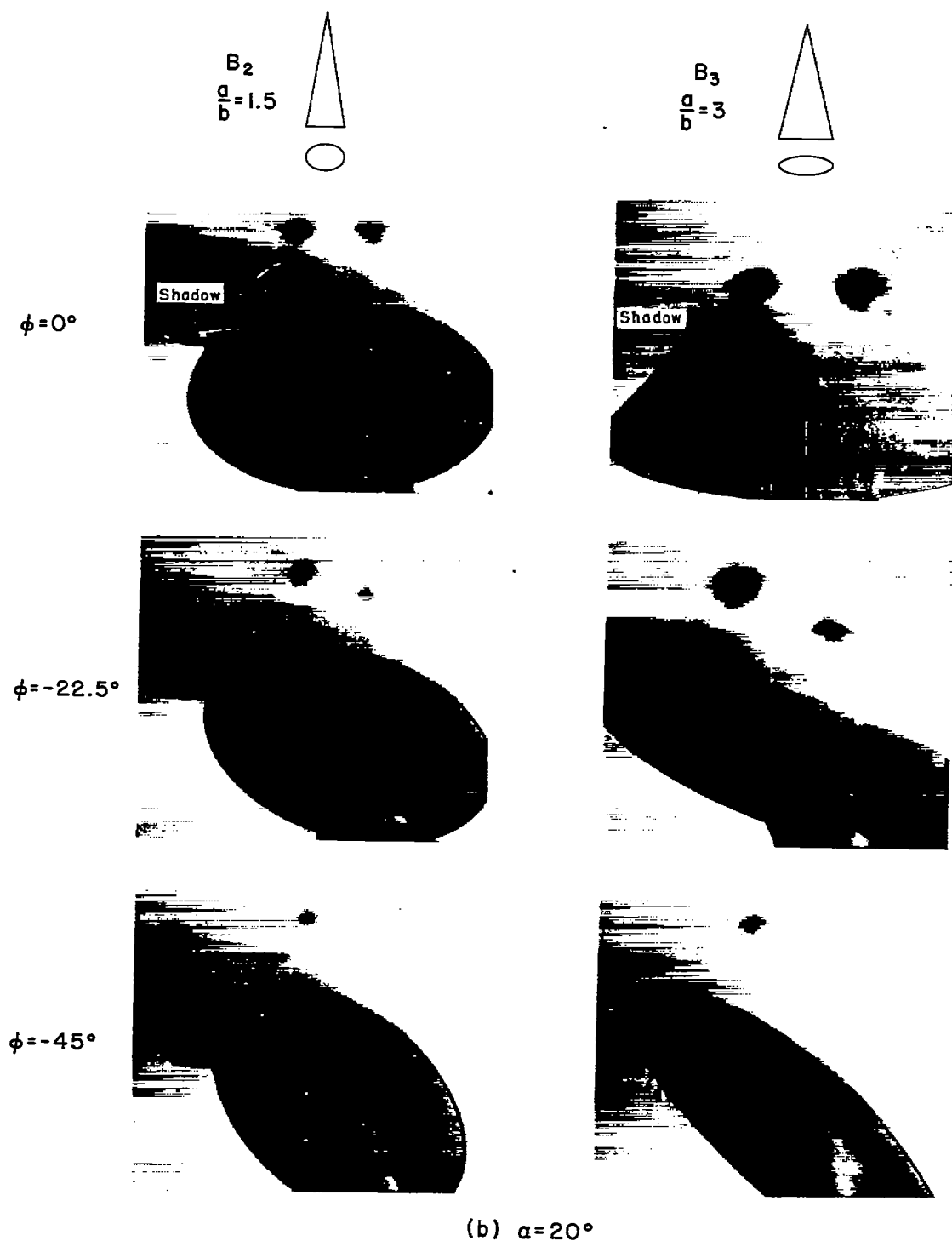
B_2
$\frac{a}{b} = 1.5$

B_3
$\frac{a}{b} = 3$

$\phi = 0°$

Shadow

Shadow

$\phi = -22.5°$

$\phi = -45°$
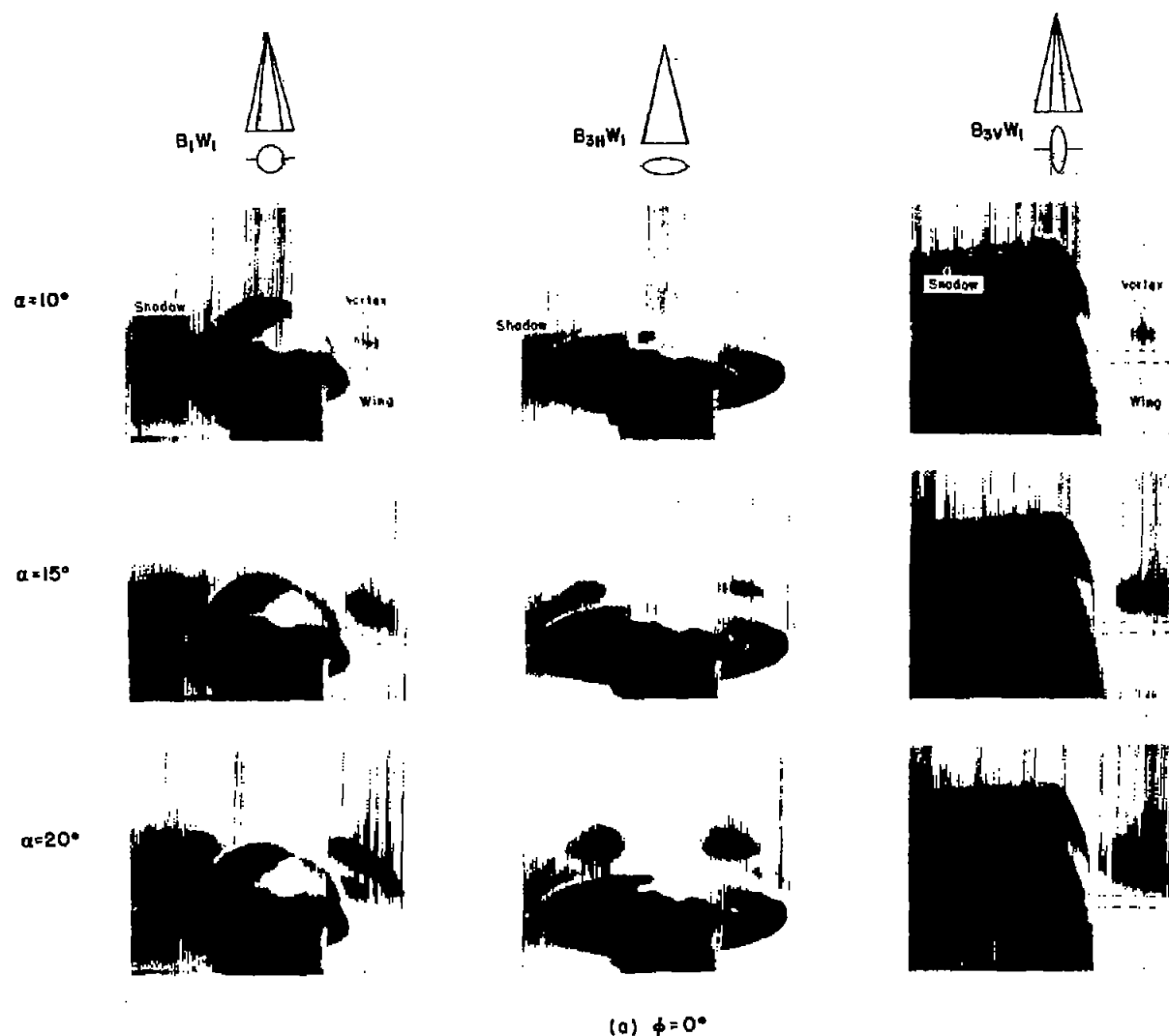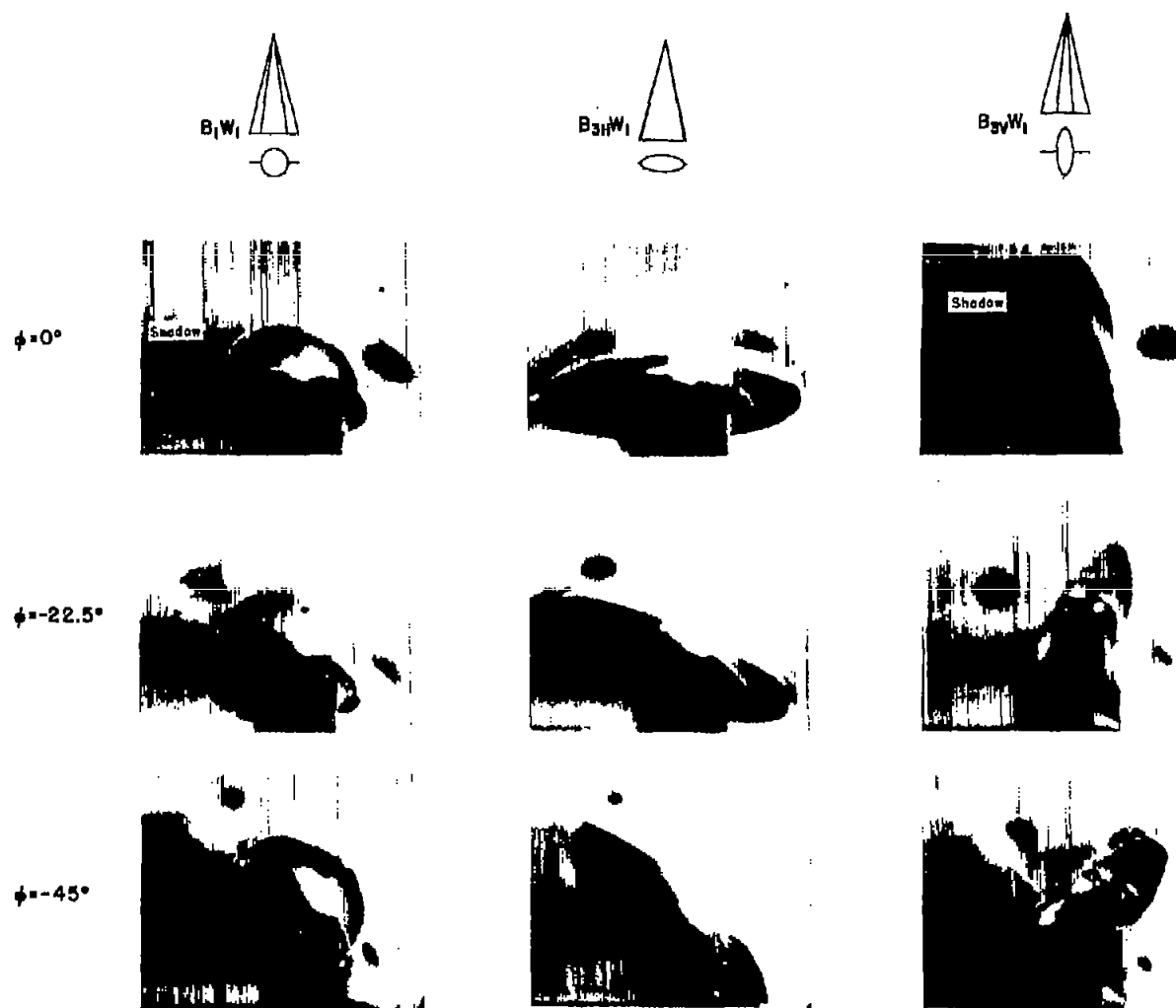
(b) $a = 20°$

Figure 19.- Concluded.

(a) $\phi = 0°$

Figure 20.- Rear views of winged elliptic cones (A = 1) showing effects of angle of attack and angle of bank on vortex patterns (with vapor-screen light plane at base); $M_\infty = 1.97$.

B_1W_1

$B_{3H}W_1$

$B_{3V}W_1$

$\phi = 0°$

Shadow

Shadow

$\phi = -22.5°$

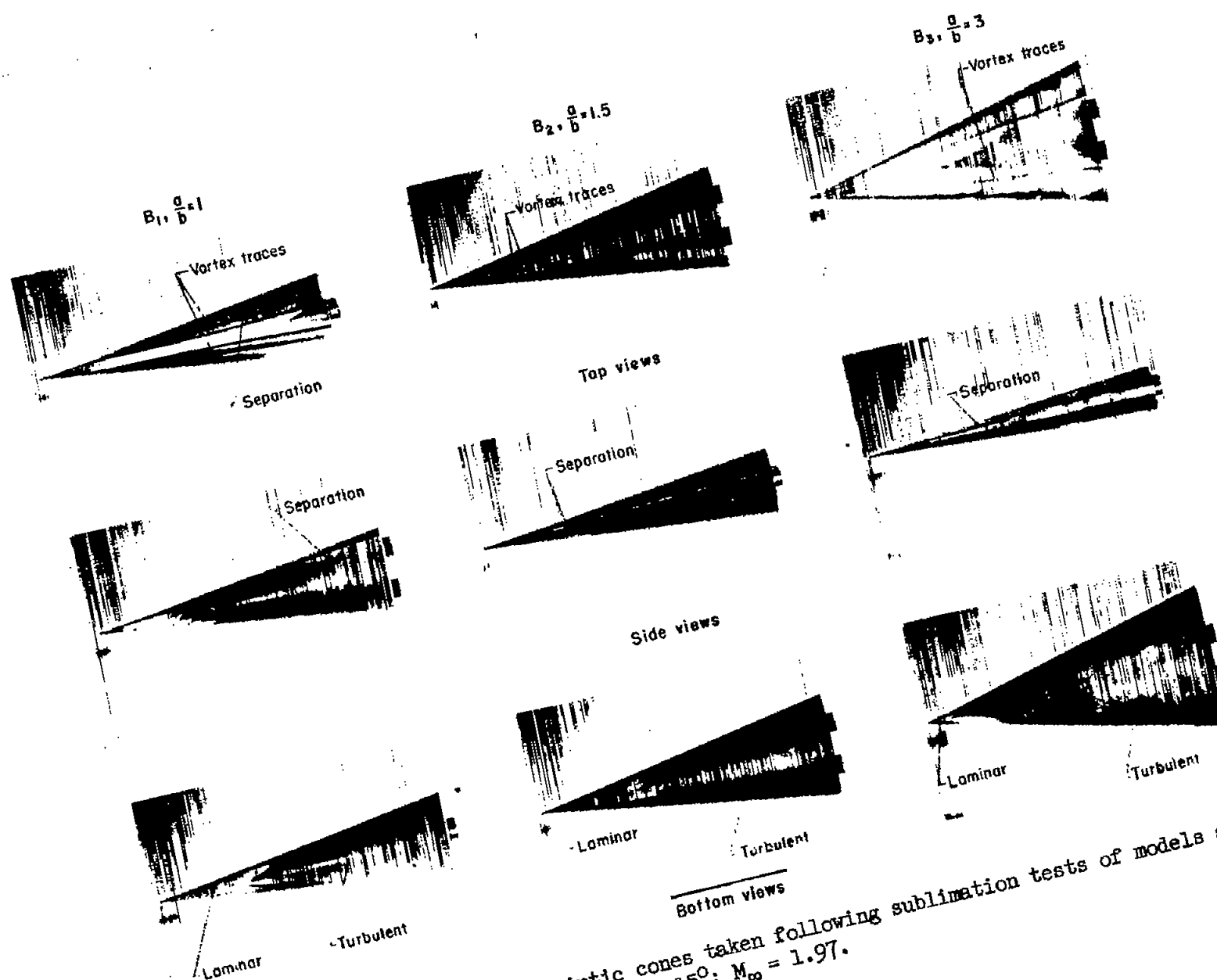$\phi = -45°$

(b) $a = 15°$

Figure 20.- Concluded.

NACA TN 4045

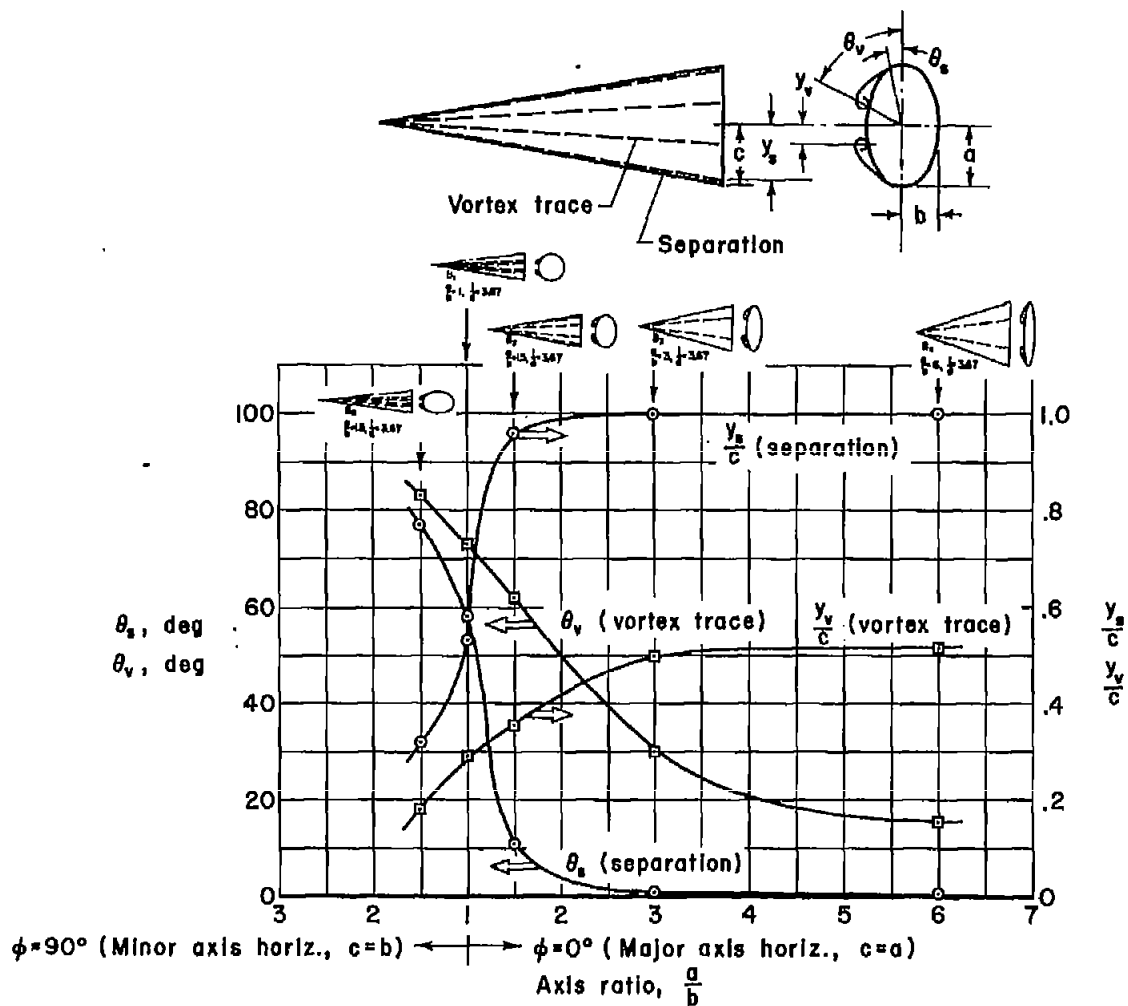Figure 21.- Photographs of elliptic cones taken following sublimation tests of models at $\alpha = 15°$; $M_\infty = 1.97$.

Figure 22.- Effect of axis ratio (a/b) on separation and vortex traces appearing on elliptic cones at $\alpha = 15°$; $l/d = 3.67$, $M_\infty = 1.97$.